

JIGSAW-GEO (1.0): Locally-orthogonal staggered unstructured grid-generation for general circulation modelling on the sphere*

Darren Engwirda^{1,2}

¹Department of Earth, Atmospheric and Planetary Sciences, Room 54-1517, Massachusetts Institute of Technology, 77 Massachusetts Avenue, Cambridge, MA 02139-4307

²NASA Goddard Institute for Space Studies, 2880 Broadway, New York, NY 10025 USA

Correspondence to: Darren Engwirda (engwirda@mit.edu)

Abstract. An algorithm for the generation of non-uniform, locally-orthogonal staggered unstructured spheroidal grids is described. This technique is designed to generate very high-quality staggered Voronoi/Delaunay meshes appropriate for general circulation modelling on the sphere, including applications to atmospheric simulation, ocean-modelling and numerical weather prediction. Using a recently developed Frontal-Delaunay refinement technique, a method for the construction of high-quality unstructured spheroidal Delaunay triangulations is introduced. A locally-orthogonal polygonal grid, derived from the associated Voronoi diagram, is computed as the staggered dual. It is shown that use of the Frontal-Delaunay refinement technique allows for the generation of very high-quality unstructured triangulations, satisfying a-priori bounds on element size and shape. Grid-quality is further improved through the application of hill-climbing type optimisation techniques. Overall, the algorithm is shown to produce grids with very high element quality and smooth grading characteristics, while imposing relatively low computational expense. A selection of uniform and non-uniform spheroidal grids appropriate for high-resolution, multi-scale general circulation modelling are presented. These grids are shown to satisfy the geometric constraints associated with contemporary unstructured C-grid type finite-volume models, including the Model for Prediction Across Scales (MPAS-O). The use of user-defined mesh-spacing functions to generate smoothly graded, non-uniform grids for multi-resolution type studies is discussed in detail.

Keywords. Grid-generation; Frontal-Delaunay refinement; Voronoi tessellation; Grid-optimisation; Geophysical fluid dynamics; Ocean modelling; Atmospheric modelling; Numerical weather prediction; Model for Prediction Across Scales (MPAS)

1 Introduction

The development of atmospheric and oceanic general circulation models based on *unstructured* numerical discretisation schemes is an emerging area of research. This trend necessitates the development of unstructured grid-generation algorithms designed to produce very high-resolution, *guaranteed-quality* unstructured triangular and polygonal meshes that satisfy non-uniform mesh-spacing distributions and embedded geometrical constraints. This study investigates the applicability

*A short version of this paper appears in the proceedings of the 24th International Meshing Roundtable (Engwirda, 2015).

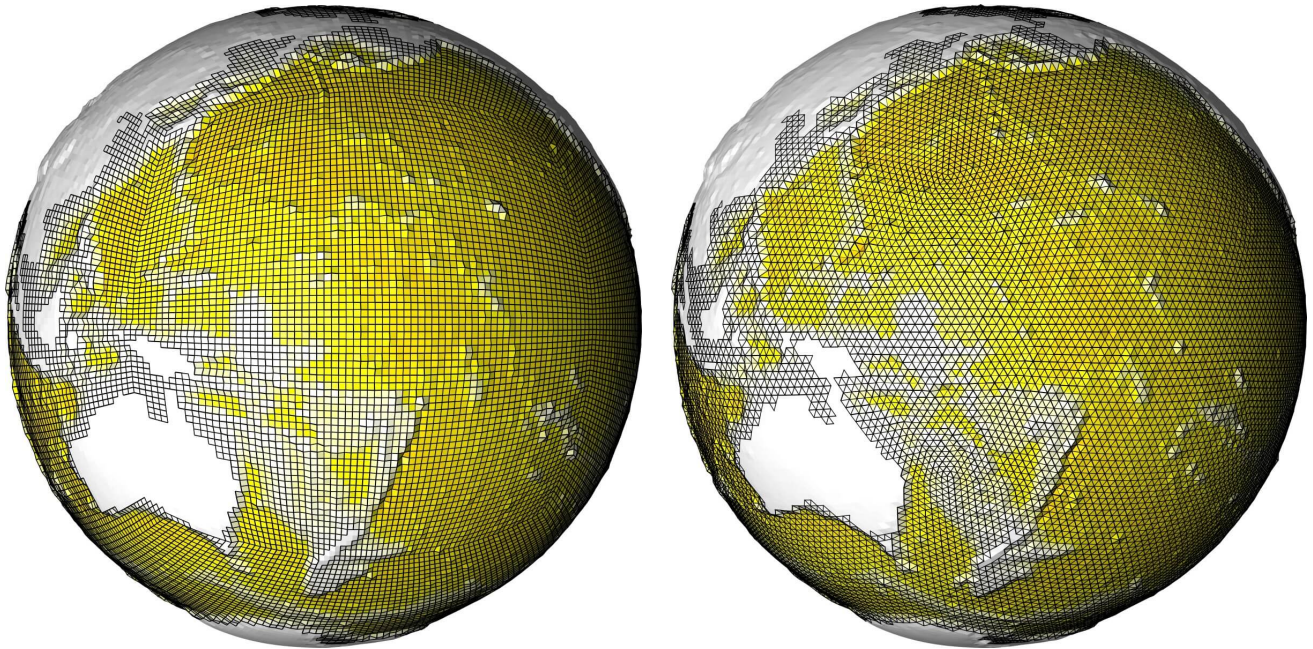


Figure 1. Conventional semi-structured meshing for the sphere, showing a regular cubed-sphere type grid (left), and a regular icosahedral class grid (right). Both grids were generated using equivalent target mean edge lengths, and are coloured according to mean topographic height at grid-cell centres. Topography is drawn using an exaggerated scale, with elevation from the reference geoid amplified by a factor of 20 in both cases.

of a recently developed surface meshing algorithm (Engwirda and Ivers, 2016; Engwirda, 2016b) based on restricted Frontal-Delaunay refinement and hill-climbing type optimisation for this task.

1.1 Semi-structured grids

While simple structured grid types for the sphere can be obtained by assembling a uniform discretisation in spherical coordinates, the resulting *lat-lon* grid is often inappropriate for numerical simulation, due to the presence of strong *grid-singularities* at the two poles. Such features manifest as local distortions in grid-quality, consisting of regions of highly distorted quadrilateral grid-cells. These low-quality elements can lead to a number of undesirable numerical effects — imposing restrictions on model time-step and stability, and compromising local spatial accuracy. As a result, a majority of current generation general circulation models are instead based on *semi-structured* quadrilateral discretisation schemes, including the *cubed-sphere* (Adcroft et al., 2004; Marshall et al., 1997; Putman and Lin, 2007) and *tri-polar* type configurations (Murray, 1996; Madec et al., 2015; Bleck, 2002).

In the cubed-sphere framework, the spherical surface is decomposed into a cube-like topology, with each of the six quadrilateral faces discretised as a structured curvilinear grid. In such an arrangement, the two strong grid-singularities of the *lat-lon* configuration are replaced by eight weak discontinuities at the cube corners, leading to significant improvements in numerical

performance. Putman and Lin (2007) present detailed discussions of techniques for the generation and optimisation of cube-sphere type grids. A regular *gnomonic-type* cubed-sphere grid is illustrated in Figure 1a. In the tri-polar grid, the present-day continental configuration is exploited to *bury* the singularities associated with a three-way polar decomposition of the sphere outside of the ocean mask. The resulting *numerically-active* subset of the grid is well-conditioned as a result. While such configurations are a popular choice for models designed for present-day Earth-based ocean studies, the generality of these methods is clearly limited. In this study, we instead pursue the development of more general-purpose techniques, applicable for both ocean and atmospheric modelling in general planetary, present-day and paleo-Earth environments.

In addition to the standard cubed-sphere and tri-polar type configurations, a second class of semi-structured spherical grid can be constructed through *icosahedral-type* decompositions (Heikes and Randall, 1995; Randall et al., 2002). In such cases, the primary grid is defined as a regular spherical triangulation, obtained through recursive bisection of the icosahedral configuration. Additionally, a staggered polygonal *dual* grid, consisting of hexagonal and pentagonal cells, is often used as a basis for finite-volume type numerical schemes. This geometrical duality is an example of the *locally-orthogonal* Delaunay/Voronoi type grid staggering that forms the basis of this paper. Icosahedral-type grids provide a near-perfect tessellation of the sphere — free of topological discontinuities and/or geometric irregularity. Such methods are applicable to both atmospheric and oceanic type simulations. A regular icosahedral-class grid is illustrated in Figure 1b.

1.2 Unstructured grids

While the semi-structured grids described previously each provide effective frameworks for uniform resolution global simulation, the development of *multi-resolution* modelling environments requires alternative techniques. A range of new general circulation models, including the Finite Element Sea Ice-Ocean Model (FESOM) (Wang et al., 2014), the Finite Volume Community Ocean Model (FVCOM) (Chen et al., 2003, 2007; Lai et al., 2010), the Stanford Unstructured Non-hydrostatic Terrain-following Adaptive Navier-Stokes Simulator (SUNTANS) (Fringer et al., 2006; Vitousek and Fringer, 2014), and the Second-generation Louvain-la-Neuve Ice-ocean Model (SLIM) (Bernard et al., 2007; Comblen et al., 2009) are based on semi-structured triangular grids, with the horizontal directions discretised according to an unstructured spherical triangulation, and the vertical direction represented as a stack of locally structured layers. The Model for Prediction Across Scales (MPAS) (Skamarock et al., 2012; Ringler et al., 2013, 2008) adopts a similar arrangement, except that a *locally-orthogonal* unstructured discretisation is adopted, consisting of both a Spherical Voronoi Tessellation (SVT) and its dual Delaunay triangulation. The use of fully unstructured representations, based on general tetrahedral and/or polyhedral grids, are also under investigation in the Fluidity framework (Ford et al., 2004a, b; Pain et al., 2005; Piggott et al., 2008). Such models all impose different requirements on the *quality* of the underlying unstructured grids, with some models, including FESOM, SLIM and Fluidity, offering additionally flexibility. In all cases though, the performance of the numerical simulation can be expected to improve with increased grid-quality — encouraging the search for optimised grid-generation algorithms. A full discussion of grid-quality constraints for general circulation modelling is presented in Section 2.

Existing approaches for unstructured grid-generation on spherical geometries have focused on a number of techniques, including: (i) the use of iterative, optimisation-type algorithms designed to construct Spherical Centroidal Voronoi Tessellations

(SCVT's) (Jacobsen et al., 2013), and (ii) the adaptation of anisotropic two-dimensional meshing techniques (Lambrechts et al., 2008) that build grids in associated parametric spaces. The MPI-SCVT algorithm (Jacobsen et al., 2013) is a massively parallel implementation of iterative Lloyd-type smoothing (Du et al., 1999) for the construction of SVCT's for use in the MPAS framework. In this approach, a set of vertices are distributed over the spherical surface and iteratively *smoothed* until
5 a high-quality Voronoi tessellation is obtained. Specifically, each iteration repositions vertices to the centroids of their associated Voronoi cells and updates the topology of the underlying spherical Delaunay triangulation. While such an approach typically leads to the generation of high-quality *centroidal* Voronoi tessellations on the sphere (SCVT's), the algorithm does not provide theoretical guarantees on minimum element quality, and often requires significant computational effort to achieve convergence. Additionally, current implementations of the MPI-SCVT algorithm do not provide a mechanism to constrain the
10 grid to embedded features, such as coastal boundaries.

Lambrechts et al. (2008) present an unstructured spherical triangulation framework using the general-purpose grid-generation package Gmsh (Geuzaine and Remacle, 2009). In this work, unstructured spherical triangulations are generated for the world ocean using a parametric meshing approach. Specifically, a triangulation of the spherical surface is generated by *mapping* the full domain (including coastlines) on to an associated two-dimensional parametric space via stereographic
15 projection. Importantly, as a result of the projection, the grids constructed in parametric space must be highly anisotropic, such that a well-shaped, isotropic triangulation is induced on the sphere. A range of existing two-dimensional anisotropic meshing algorithms are investigated, including Delaunay-refinement, advancing-front, and adaptation-type approaches. In particular, the algorithm is designed to ensure a faithful representation of complex coastal boundary conditions. While a detailed model of such constraints is often neglected in global simulations, resolution of these features is a key factor for regional and coastal
20 models. Several algorithms support the generation of unstructured two-dimensional grids for such domains, including the ADmesh package (Conroy et al., 2012) and the Stomel library (Holleman et al., 2013).

The current study explores the development of a new algorithm for the generation of high-resolution, guaranteed-quality spheroidal Delaunay triangulations and associated Voronoi tessellations — appropriate for a range of unstructured-grid type general circulation models. In this work, meshes are generated on the spheroidal surface directly, without need for local param-
25 eterisation or projection. Such an approach will be shown to exhibit significant flexibility — immune to issues of coordinate singularity and/or continental configuration. The applicability of this approach to grid-generation for imperfect spheres, including oblate spheroids and general ellipsoidal surfaces is also explored. Overall, significant effort is invested to develop techniques designed to produce very high-quality multi-resolution grids appropriate for contemporary unstructured C-grid type models, such as the MPAS framework. The paper is organised as follows: an overview of grid-generation for general circulation mod-
30 elling is presented in Section 2, outlining various constraints and minimum requirements on grid-quality. A description of the Frontal-Delaunay refinement and hill-climbing type optimisation algorithms is given in Sections 3 and 4. A set of uniform and non-uniform grids appropriate for high-resolution, multi-scale general circulation modelling are presented Section 5, alongside an analysis of computational performance and optimality. Avenues for future work are outlined in Section 6.

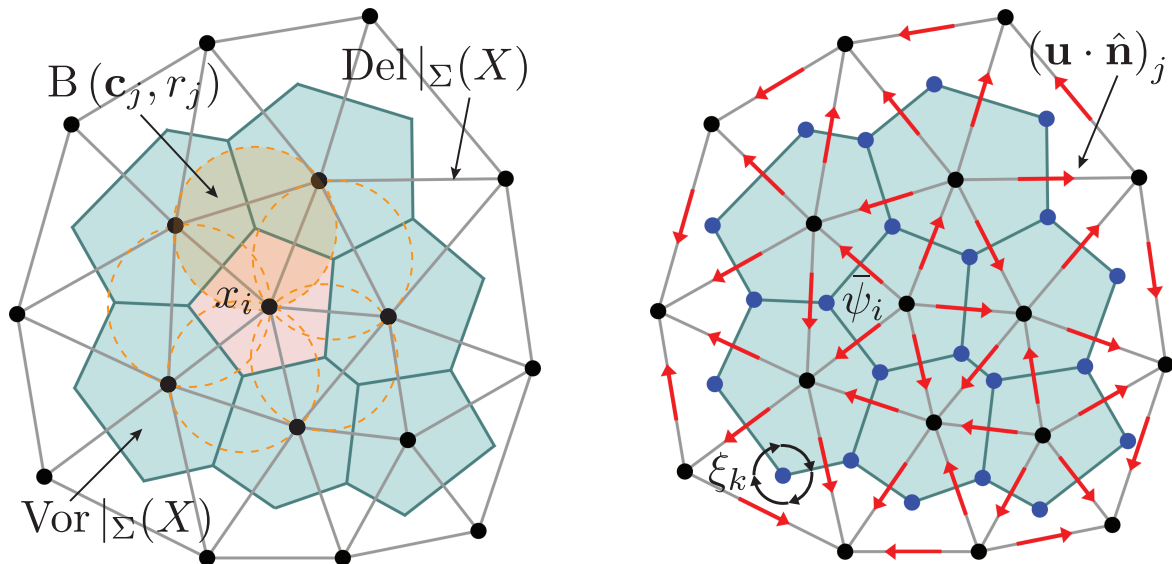


Figure 2. Construction of the staggered surface Voronoi control-volumes, illustrating: (left) locally-orthogonal Voronoi/Delaunay staggering, and (right) an associated unstructured C-grid type numerical discretisation scheme, as per the MPAS model. The formulation is a combination of conservative *cell-centred* tracer quantities $\bar{\psi}_i$, *edge-centred* normal velocity components $(\mathbf{u} \cdot \hat{\mathbf{n}})_j$, and auxiliary *vertex-centred* vorticity variables ξ_k .

2 Grid-generation for general-circulation modelling

Numerical formulations for large-scale atmospheric and/or oceanic general circulation modelling are often based on a *staggered* grid configuration, with quantities such as fluid pressure, geopotential, and density discretised using a primary control-volume, and the fluid velocity field and vorticity distribution represented at secondary, spatially distinct grid-points. In the context of standard structured grid types, various staggered arrangements are described by the well-known Arakawa schemes (Arakawa and Lamb, 1977).

The development of general circulation models based on unstructured grid types is an emerging area of research, and, as a result, a variety of numerical formulations are currently under investigation. In this study, the development of *locally-orthogonal* grids appropriate for staggered unstructured C-grid type numerical schemes are pursued, as these methods are thought to represent the most logical extension of the conventional structured Arakawa-type techniques to the unstructured setting. Such formulations require that grids satisfy a *local-orthogonality* constraint, with adjacent grid-cell edges in the primary and secondary control-volumes required to be mutually perpendicular. In the unstructured setting, it is known that the Delaunay triangulation and Voronoi tessellation constitute a locally-orthogonal staggered dual, leading to a natural framework for the construction of such unstructured meshes.

Consisting of a set of (convex) polygonal grid-cells centred on each vertex in the underlying triangulation, the surface Voronoi diagram $\text{Vor}|_{\Sigma}(X)$ obeys a number of local orthogonality constraints. Specifically, grid-cell edges in the Voronoi

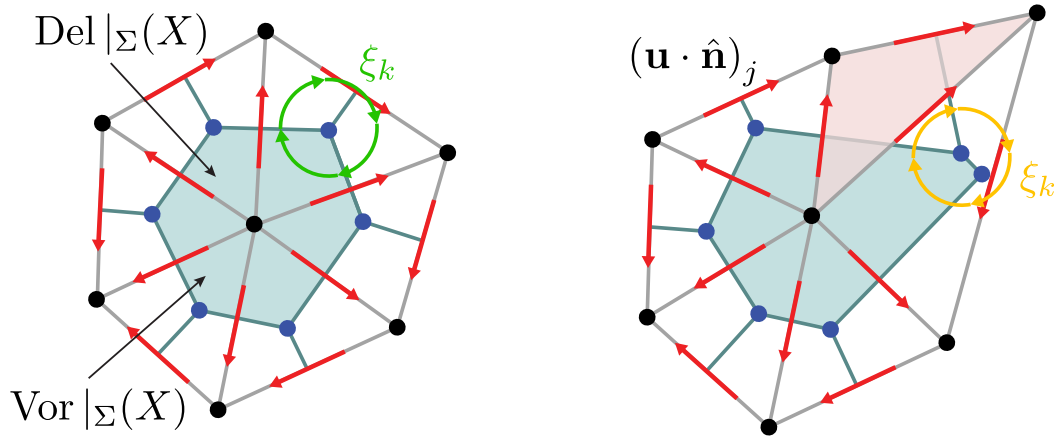


Figure 3. Comparison of *well-centred* and *poorly-staggered* Voronoi/Delaunay dual grids, from left to right, respectively. In the *well-centred* configuration, each vertex of the Voronoi polygon lies within the interior of its associated Delaunay triangle. A conservative computation of the vertex-centred vorticity variables can therefore be achieved using the three velocity components adjacent to each circumcentre. In the *poorly-staggered* configuration, one Voronoi vertex lies outside its associated triangle (shaded). The associated Voronoi and Delaunay edges do not intersect as a result, and the triangle-based vorticity reconstruction is no longer valid. Note that the quality of the triangulation here is not pathological, with all angles bounded below $\theta_f \leq 120^\circ$. The construction of fully *well-centred* grids can be seen as a difficult problem as a result, requiring the assembly of very high-quality Delaunay triangulations.

tessellation are guaranteed to be perpendicular to their associated edges in the underlying Delaunay triangulation, passing through the Delaunay-edge midpoints. Additionally, in the case of perfectly *regular* and *centroidal* tessellations, the Delaunay-edges are guaranteed to pass through the midpoints of their associated Voronoi duals. Voronoi grid-cells are formed as the convex-hull of the incident element *circumcentres* associated with the set of surface triangles adjacent to each vertex. Example

5 Voronoi/Delaunay type unstructured grid staggering is illustrated in Figure 2.

While detailed comparisons of particular numerical discretisation schemes lie outside the scope of the current study, brief comments regarding the benefits of locally-orthogonal grid-staggering arrangements are made. Pursuing an unstructured variant of the widely-used Arakawa C-grid, the placement of fluid pressure, geopotential and density degrees-of-freedom within the primary Voronoi control-volumes, and orthogonal velocity vectors on Delaunay-edges achieves a similar configuration. Such

10 an arrangement facilitates construction of a standard conservative finite-volume type scheme for the transport of fluid properties and a *mimetic* class (Lipnikov et al., 2014; Bochev and Hyman, 2006) finite-difference formulation for the evolution of velocity components. Additionally, exploiting alignment with Delaunay-edges, a conservative evaluation of the fluid vorticity can be made on the staggered Delaunay triangles. Overall, this scheme is known to possess a variety of desirable conservation properties, conserving mass, potential vorticity and enstrophy, and preserving geostrophic balance. This *unstructured C-grid*

15 scheme is currently employed in the Model for Prediction Across Scales (MPAS) for both atmospheric and oceanic modelling (Skamarock et al., 2012; Ringler et al., 2013, 2010). See Figure 2 for additional details.

While numerically elegant, such unstructured C-grid schemes impose a heavy-burden on the quality of the underlying unstructured grid, requiring not only that grids be locally-orthogonal, but also *well-centred* and mutually *centroidal*. The *well-centred*-ness and *centroidal*-ness of an unstructured grid are constraints related to the nature of the staggering between the primary and secondary grid-cells. Specifically, a grid is *well-centred* when all dual Voronoi vertices lie within the interior of their associated Delaunay triangles. Such a constraint guarantees that adjacent Delaunay and Voronoi edges intersect, and, in the context of the unstructured C-grid scheme described previously, guarantees that a consistent stencil exists for the reconstruction of the discrete vorticity variable. In practice, the construction of well-centred grids is known to be particularly onerous (VanderZee et al., 2008; Vanderzee et al., 2010), requiring that the triangulation consist of all-acute elements. See Figure 3 for additional detail.

Unstructured grids are *centroidal* when their primary and secondary vertices lie at the centres-of-mass of their associated dual grid-cells, with the vertices of the Voronoi polygons lying at the centroids of the Delaunay triangles and visa-versa. Such a condition is effectively an implicit constraint on the *regularity* of the grid, with an increase in the *centroidal*-ness of a grid associated with improvements in the shape of its Delaunay triangles and Voronoi polygons. Centroidal grids typically lead to high-quality numerical discretisations, with grids containing near-perfect element configurations achieving *optimal* convergence rates. The unstructured C-grid scheme outlined previously is known to achieve fully second-order accurate convergence when applied to centroidal Voronoi grids (Ringler et al., 2010).

While a number of unstructured grid-generation algorithms currently exist, as outlined in Section 1, I am not aware of any that are successful in generating the very high-quality *locally-orthogonal*, *well-centred* and *centroidal* grids required by unstructured C-grid type general circulation models. As a result, throughout the remainder of this paper, the development of methods for the generation of such staggered Delaunay/Voronoi tessellations is pursued in detail.

2.1 Grid-quality metrics

Before moving on to a detailed description of the grid-generation algorithm itself, a number of mesh-quality metrics are first introduced.

Definition 1. (radius-edge ratio) Given a surface triangle $f_i \in \text{Del}|_{\Sigma}(X)$, its *radius-edge* ratio, $\rho(f_i)$, is given by

$$\rho(f_i) = \frac{r_i}{\|\mathbf{e}_{\min}\|}, \quad (1)$$

where r_i is the radius of the circumscribing ball associated with f_i and $\|\mathbf{e}_{\min}\|$ is the length of its shortest edge.

The radius-edge ratio is a measure of element shape-quality. It achieves a minimum, $\rho(f_i) = 1/\sqrt{3}$ for equilateral triangles and increases toward $+\infty$ as elements tend toward degeneracy. The radius-edge ratio is directly related to the minimum plane-angle θ_{\min} between adjacent edges in the triangulation, such that $\rho(f_i) = \frac{1}{2}(\sin(\theta_{\min}))^{-1}$. Due to the summation of angles in a triangle, given a minimum angle θ_{\min} the largest angle θ_{\max} is also clearly bounded, such that $\theta_{\max} \leq \pi - 2\theta_{\min}$.

Definition 2. (area-length ratio) Given a surface triangle $f_i \in \text{Del}|_{\Sigma}(X)$, its *area-length* ratio, $a(f_i)$, is given by

$$a(f_i) = \frac{4\sqrt{3}}{3} \frac{A_f}{\|\mathbf{e}_{\text{rms}}\|^2}, \quad (2)$$

where A_f is the signed-area of f_i and $\|\mathbf{e}_{\text{rms}}\|$ is the root-mean-square edge length.

The area-length ratio is a robust, scalar measure of element shape-quality, and is typically normalised to achieve a score of +1 for ideal elements. The area-length ratio decreases with increasing distortion, achieving a score of +0 for degenerate elements and -1 for tangled elements with reversed orientation.

5 **Definition 3.** (relative edge-length) Given an edge in the surface tessellation $e_j \in \text{Del}|_{\Sigma}(X)$, its *relative edge-length*, $h_r(e_j)$, is given by

$$h_r(e_j) = \frac{\|\mathbf{e}_j\|}{\bar{h}(\mathbf{x}_m)}, \quad (3)$$

where $\|\mathbf{e}_j\|$ is the length of the j -th edge and $\bar{h}(\mathbf{x}_m)$ is the value of the mesh-spacing function sampled at the edge midpoint.

The relative-length distribution $h_r(e_j)$ is a measure of mesh-spacing conformance, expressing the ratio of actual-to-desired edge-length for all edge-segments in $\text{Del}|_{\Sigma}(X)$. A value of $h_r(e_j) = 1$ indicates perfect mesh-spacing conformance.

3 A restricted Frontal-Delaunay refinement algorithm for spheroidal surfaces

The task is to generate very high-resolution, guaranteed-quality unstructured Delaunay triangulations for planetary atmospheres and/or oceans. These grids will form a baseline for the hill-climbing mesh-optimisation techniques presented in subsequent sections. In addition to bounds on minimum element quality, these grids are also required to satisfy general non-uniform, user-
15 defined mesh-spacing constraints. In this work, the applicability of a recently developed Frontal-Delaunay surface meshing algorithm (Engwirda and Ivers, 2016; Engwirda, 2016b) is investigated for this task.

An unstructured Delaunay triangulation of the reference spheroid associated with a general planetary geometry is sought. In a general form, this reference surface can be expressed as an axis-aligned triaxial ellipsoid

$$\sum_{i=1}^3 \left(\frac{x_i}{r_i} \right)^2 = 1, \quad (4)$$

20 where the x_i 's are the Cartesian coordinates in a locally aligned coordinate system, and the scalars $r_i > 0$ are its principal radii. Such a definition can be used to represent ellipsoidal surfaces in general position, based on the application of additional rigid-body translations and rotations. Note that while grid-generation for global climate modelling is often restricted to spherical surfaces, setting $r_{1,2,3} = 6371\text{km}$, this formulation supports mesh-generation on general spheroidal and ellipsoidal domains.

3.1 Preliminaries

25 In this work, attention is restricted to the generation of locally-orthogonal staggered unstructured grids, consisting of Delaunay triangulations and their associated Voronoi duals. A full account of such structures is not presented here, instead, the reader is referred to the detailed theoretical exposition presented in, for example, Cheng et al. (2013).

The Delaunay triangulation $\text{Del}(X)$ associated with a set of points $X \in \mathbb{R}^d$ is characterised by the so-called *empty-circle* criterion — requiring that the set of circumscribing spheres $B(\mathbf{c}_i, r_i)$ associated with each Delaunay triangle $\tau_i \in \text{Del}(X)$ be

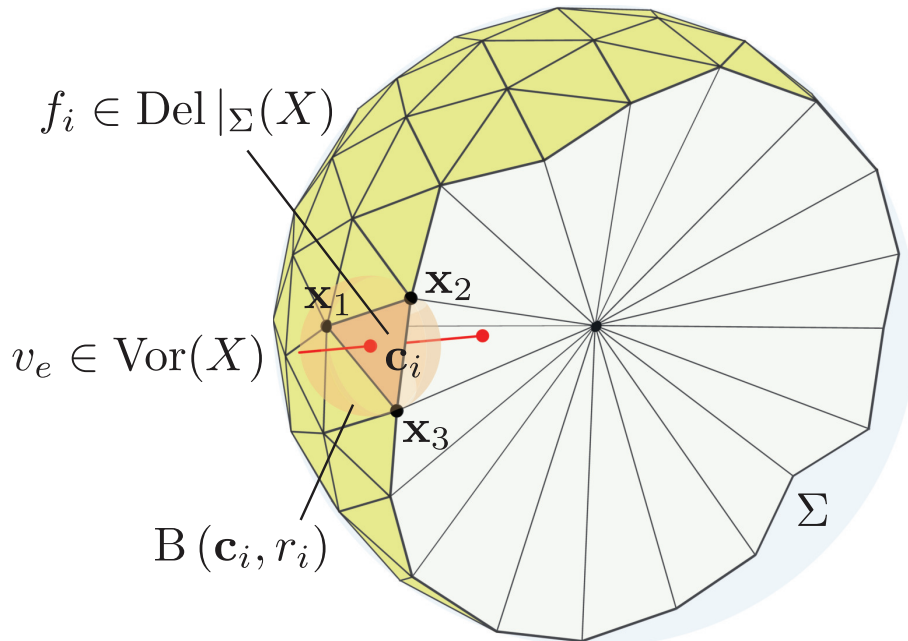


Figure 4. Illustration of the geometrical predicates used to define the restricted Delaunay surface triangles $f_i \in \text{Del}|_{\Sigma}(X)$, showing details of the intersecting Voronoi edge $v_e \in \text{Vor}(X)$ associated with the surface triangle $f_i \in \text{Del}|_{\Sigma}(X)$ and its associated surface-ball $B(\mathbf{c}_i, r_i)$. Note that the full three-dimensional Delaunay tessellation $\text{Del}(X)$ is a tetrahedral complex that fills the interior of the spheroid.

empty of all points other than its own vertices. It is well known that for tessellations restricted to two-dimensional manifolds, the Delaunay triangulation leads to a maximisation of the minimum enclosed angle in the grid (Cheng et al., 2013). Such behaviour is clearly beneficial when seeking to construct high quality triangular meshes.

The Voronoi tessellation $\text{Vor}(X)$ is the so-called *geometric-dual* associated with the Delaunay triangulation, consisting of a set of convex polygonal cells formed by connecting the centres of adjacent circumscribing balls — the so-called element *circumcentres* \mathbf{c}_i 's. The Voronoi tessellation represents a *closest-point map* for the points in X , with each Voronoi cell $v_e \in \text{Vor}(X)$ defining the convex region adjacent to a given vertex $\mathbf{x}_i \in X$ for which \mathbf{x}_i is the nearest point. Importantly, the Voronoi/Delaunay grid staggering, defines a *locally-orthogonal* arrangement, in which grid-cell edges in the Voronoi tessellation are orthogonal to adjacent edges in the underlying Delaunay triangulation.

10 3.2 Restricted Delaunay triangulation

In this study, grid-generation is carried out on the surface of the spheroidal geometry directly by making use of so-called *restricted* Delaunay mesh generation techniques. Specifically, given a reference surface Σ , grid-generation proceeds to discretise the surface into a mesh of triangles. In the restricted Delaunay framework, a full-dimensional Delaunay triangulation $\text{Del}(X)$ (i.e. a tetrahedral tessellation) is maintained, with the surface triangulation represented as a subset of tetrahedral faces. The *re-*

stricted Delaunay surface-complex is said to be *embedded* in $\text{Del}(X)$ as a result. Use of this fully three-dimensional approach elides any reliance on local parametric projections.

Definition 4. (restricted Delaunay tessellation) Let Σ be a smooth surface embedded in \mathbb{R}^3 . Let $\text{Del}(X)$ be a full-dimensional Delaunay tetrahedralisation of a point-wise sample $X \subseteq \Sigma$ and $\text{Vor}(X)$ be the associated Voronoi tessellation. The *restricted*
 5 *Delaunay surface triangulation* $\text{Del}|_{\Sigma}(X)$ is a sub-complex of $\text{Del}(X)$ including any triangle $f_i \in \text{Del}(X)$ associated with an *intersecting* Voronoi edge $\mathbf{v}_e \in \text{Vor}(X)$ where $\mathbf{v}_e \cap \Sigma \neq \emptyset$.

The development of restricted Delaunay techniques for general mesh-generation applications has been the subject of previous research, and a detailed discussion of such concepts is not presented here as a result. The reader is referred to the original work of Edelsbrunner and Shah (1997) or the detailed reviews presented in Cheng et al. (2013) for additional details and mathematical
 10 background.

In the context of this work, it is sufficient to note that the restricted Delaunay triangulation framework provides a convenient mechanism to identify elements in the surface triangulation $\text{Del}|_{\Sigma}(X)$. In practice, implementation of this scheme requires the definition of a single *geometrical-predicate*, designed to compute intersections between Voronoi edges and the underlying surface. Triangles associated with non-empty intersections $\text{Vor}|_f(X) \cap \Sigma \neq \emptyset$ form part of the surface mesh. In this study, this
 15 predicate is computed analytically, following standard spheroidal trigonometric manipulations, as detailed in Appendix A. See Figure 4 for detailed schematics.

3.3 Mesh-spacing functions

Local mesh density can be controlled via user-specified mesh-spacing functions $\bar{h}(\mathbf{x}) : \mathbb{R}^3 \rightarrow \mathbb{R}^+$ that define the *target* edge-length values over the surface Σ . In this work, mesh-spacing functions are specified as a discrete set of target values $\bar{h}_{i,j}$,
 20 defined on a simple background ‘lat-lon’ grid \mathcal{G} . The continuous mesh-spacing function $\bar{h}(\mathbf{x})$ is reconstructed using bilinear interpolation. As will be illustrated in subsequent sections, such an approach provides support for a wide range of mesh-spacing definitions, including distributions derived from high-resolution topographic data (Amante and Eakins, 2009) or solution-adaptive metrics.

In order to generate high-quality grids, it is necessary to ensure that the imposed mesh-spacing function is sufficiently
 25 smooth. Rather than requiring the user to accommodate such constraints, a Lipschitz smoothing process is adopted here. Following the work of Persson (2006), a *gradient-limited* mesh-spacing function $\bar{h}'(\mathbf{x})$ is constructed, by limiting the allowable spatial fluctuation over each element in the background grid \mathcal{G} . In this study, a scalar smoothing parameter $g \in \mathbb{R}^+$ is used to limit variation, such that

$$\bar{h}'(\mathbf{x}_i) \leq \bar{h}'(\mathbf{x}_j) + g \cdot \text{dist}(\mathbf{x}_i, \mathbf{x}_j), \quad (5)$$

30 for all adjacent vertex pairs $\mathbf{x}_i, \mathbf{x}_j$ in \mathcal{G} . The gradient-limited mesh-spacing function $\bar{h}'(\mathbf{x})$ becomes more uniform as $g \rightarrow 0$. In this work, maximum gradient constraints are implemented following a *fast-marching* method, as described in Persson (2006).

Algorithm 1 Restricted Frontal-Delaunay Refinement

<p>1: function DELFRONT($\Sigma, \bar{\rho}, \bar{h}(\mathbf{x}), \text{Del} _{\Sigma}(X)$)</p> <p>2: Place 12 vertices on the spheroidal surface Σ to form a regular icosahedron. Initialise the full Delaunay complex $\text{Del}(X)$ and the restricted surface triangulation $\text{Del} _{\Sigma}(X)$.</p> <p>3: while ($\exists \text{BADTRIANGLE}(\text{Del} _{\Sigma}(X))$) do</p> <p>4: Find the worst bad <i>frontal</i> triangle in the surface triangulation $f_i \leftarrow \text{Del} _{\Sigma}(X)$.</p> <p>5: Call $\mathbf{x}_i \leftarrow \text{OFFCENTRE}(f_i)$ to form the new off-centre vertex \mathbf{x}_i, designed to eliminate the bad triangle f_i.</p> <p>6: Push $\text{Del}(X) \leftarrow \mathbf{x}_i$ and update the restricted surface triangulation $\text{Del} _{\Sigma}(X)$.</p> <p>7: end while</p> <p>8: return surface triangulation object $\text{Del} _{\Sigma}(X)$.</p> <p>9: end function</p> <p>1: function BADTRIANGLE(f)</p> <p style="padding-left: 2em;">if ($h(f) > \bar{h}(\mathbf{x}_f)$) return TRUE</p> <p style="padding-left: 2em;">if ($\rho_2(f) > \bar{\rho}$) return TRUE</p> <p style="padding-left: 2em;">else return FALSE</p> <p>3: end function</p>	<p>1: function OFFCENTRE(f, \mathbf{x})</p> <p>2: Form the restricted triangle circumcentre $\mathbf{x}_c \leftarrow \text{Vor} _f(X) \cap \Sigma$ and the associated surface ball $B = \text{SDB}(f)$.</p> <p>3: Find the minimum length edge e in the triangle f. Edge e is the <i>frontal</i> segment.</p> <p>4: Place the <i>size-optimal</i> point \mathbf{x}_h along the arc $\text{Vor} _e(X) \cap \Sigma$ to satisfy local spacing constraints $\bar{h}(\mathbf{x})$.</p> <p>5: Place the <i>shape-optimal</i> point \mathbf{x}_θ along the arc $\text{Vor} _e(X) \cap \Sigma$ to satisfy minimum angle constraints $\rho(f) \leq \bar{\rho}$.</p> <p>6: Compute the distances $d_h = \text{dist}(\mathbf{x}_e, \mathbf{x}_h)$ and $d_\theta \leftarrow \text{dist}(\mathbf{x}_e, \mathbf{x}_\theta)$, where \mathbf{x}_e is the midpoint of the short edge e.</p> <p>7: Set \mathbf{x} to the point $\{\mathbf{x}_h, \mathbf{x}_\theta\}$ of minimum distance d_j, such that $d_j \geq \frac{1}{2}\ \mathbf{e}\$. Fall-back to $\mathbf{x} \leftarrow \mathbf{x}_c$ if $\{\mathbf{x}_h, \mathbf{x}_\theta\}$ do not satisfy constraints.</p> <p>8: return off-centre vertex \mathbf{x}.</p> <p>9: end function</p>
---	---

3.4 Restricted Frontal-Delaunay refinement

In this study, a high-quality triangular surface mesh is generated on the spheroidal reference surface (4) using a *Frontal-Delaunay* variant of the conventional restricted Delaunay-refinement algorithm (Boissonnat and Oudot, 2003, 2005; Jamin et al., 2015; Cheng et al., 2007, 2010). This technique is described by the author in detail in Engwirda and Ivers (2016); Engwirda (2016b) and differs from standard Delaunay-refinement approaches in terms of the strategies used for the placement of new Steiner vertices. Specifically, the Frontal-Delaunay algorithm employs a generalisation of various *off-centre* type point-placement techniques (Rebay, 1993; Erten and Üngör, 2009), designed to position vertices such that that element-quality and mesh-size constraints are satisfied in a *locally-optimal* fashion. Previous studies have shown that such an approach typically leads to substantial improvements in mean element-quality and mesh smoothness.

While a variety of grid-generation algorithms for the surface meshing problem have been described previously (e.g. Frey and George, 2007; Rypl and Krysl, 1997; Schreiner et al., 2006; Löhner, 1996), the restricted Frontal-Delaunay method presented here has been found to offer a unique combination of characteristics — combining the smooth, high quality grid-generation capabilities of an advancing-front approach, with the theoretical robustness and provable guarantees associated with conventional Delaunay-refinement techniques. Specifically, the Frontal-Delaunay approach presented here is known to generate grids

with very high mean element quality, bounded minimum and maximum angles, tight conformance to grid-spacing constraints, and provable guarantees on topological consistency and convergence. A full description of the algorithm, including detailed discussions of its theoretical foundations and proofs of worst-case grid-quality bounds, can be found in Engwirda and Ivers (2016); Engwirda (2016b).

- 5 Given a user-defined mesh-spacing function $\bar{h}(\mathbf{x})$ and an upper-bound on the element *radius-edge* ratios $\bar{\rho} \geq 1$, the Frontal-Delaunay algorithm proceeds to sample the spheroidal surface Σ by refining any surface triangle that violates either the mesh-spacing or element-quality constraints. The full algorithm is described in Algorithm 1, and detailed snap-shots of the refinement process are shown in Figure 5. The surface is seeded with a set of twelve vertices to form a standard icosahedron. Refinement then proceeds to insert a new Steiner vertex at the *off-centre* refinement point associated with each given element to be *elim-*
- 10 *inated*. Refinement continues until all constraints are satisfied. The refinement process is priority scheduled, with triangles $f_i \in \text{Del}|_{\Sigma}(X)$ ordered according to their radius-edge ratios $\rho(f_i)$. This ordering ensures that the element with the *worst* ratio is refined at each iteration. Additionally, triangles are subject to a *frontal* filtering — requiring that a low-quality element be adjacent to a *converged* triangle before being considered for refinement. This logic helps the algorithm mimic the behaviour of *advancing-front* type algorithms, with new vertices and elements expanding from initial seeds. Upon termination, the resulting
- 15 surface triangulation is guaranteed to contain nicely shaped elements, satisfying both the radius-edge constraints $\rho(f_i) \leq \bar{\rho}$ and mesh-spacing bounds $h(f_i) \leq \bar{h}(\mathbf{x}_f)$ for all surface triangles $f_i \in \text{Del}|_{\Sigma}(X)$ in the mesh. Setting $\bar{\rho} = 1$ guarantees that element angles are bounded, such that $30^\circ \leq \theta_f \leq 120^\circ$, ensuring that the grid does not contain any highly distorted elements.

3.5 Off-centre point-placement

The performance of the Frontal-Delaunay algorithm hinges on the use of *off-centre* refinement rules — locally-optimal point-

20 placement strategies designed to create very high-quality vertex distributions. A set of candidate off-centre points are considered at each new vertex insertion. Type I vertices, \mathbf{x}_c , are equivalent to conventional element circumcentres (positioned at the centre of the associated surface balls), and are used to preserve global convergence. Type II vertices, \mathbf{x}_h , are so-called *size-optimal* points, and are designed to satisfy grid-spacing constraints in a locally optimal fashion. Type III vertices, \mathbf{x}_θ , are so-called *shape-optimal* points, and are designed to ensure minimum-angle bounds are satisfied in a worst-first manner. The

25 Type II and Type III strategies employed here can be seen as a generalisation of the two-dimensional off-centre techniques presented by Rebay (1993) and Erten and Üngör (2009), respectively. See Figure 6 for additional detail.

Given a low-quality triangle $f_i \in \text{Del}|_{\Sigma}(X)$, the Type II and Type III vertices \mathbf{x}_h and \mathbf{x}_θ are positioned along the intersection of an adjacent segment of the Voronoi complex and the spheroidal surface. This intersection $\text{Vor}|_e(X) \cap \Sigma$, defines a *frontal-curve* inscribed on Σ — a *locally-optimal* geodesic segment on which to insert new vertices. Here, $\text{Vor}|_e(X)$ is the

30 polygonal face of the Voronoi complex associated with the short edge $e_0 \in f_i$. In the context of conventional advancing-front type methods, the edge e_0 would denote the current *frontal-segment* about which vertex insertion occurs.

The points \mathbf{x}_h and \mathbf{x}_θ are positioned to form new candidate triangles about the frontal edge e_0 , such that local constraints are satisfied optimally. The size-optimal point \mathbf{x}_h is positioned to adhere to local grid-spacing constraints $\bar{h}(\mathbf{x})$, with the altitude of the new triangle candidate calculated to define correctly sized edges, such that $\|\mathbf{e}_1\| \leq \bar{h}(\mathbf{m}_1)$ and $\|\mathbf{e}_2\| \leq \bar{h}(\mathbf{m}_2)$, where

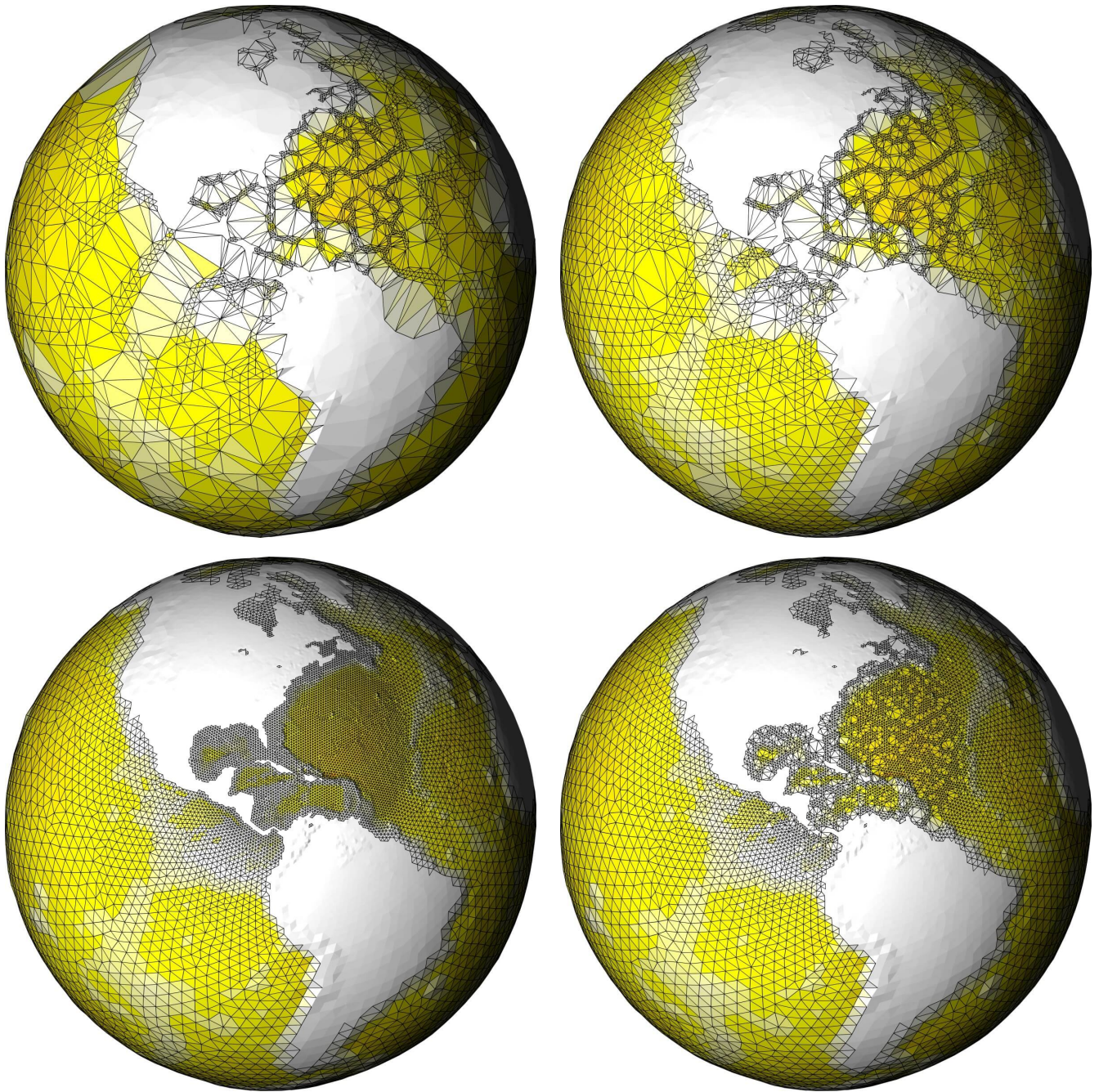


Figure 5. Progress of the Frontal-Delaunay refinement algorithm, clockwise from top-left. New vertices are inserted incrementally until all constraints on element-shape and edge-length are satisfied globally. In contrast with standard advancing-front type grid-generation techniques, new vertices are inserted according to a *greedy* priority-schedule. Grid-generation proceeds along a pseudo *space-filling* trajectory as a result.

the \mathbf{m}_i 's are the edge midpoints. These constraints can be solved for an associated altitude

$$a_h = \min(a_h^*, \sqrt{3}/2\bar{h}), \quad \text{where:} \quad a_h^* = \sqrt{\bar{h}^2 - \frac{1}{2}\|\mathbf{e}_0\|^2}, \quad \bar{h} = \frac{1}{2}(\bar{h}(\mathbf{m}_1) + \bar{h}(\mathbf{m}_2)) \quad (6)$$

Similarly, the shape-optimal point is positioned to adhere to minimum angle constraints, sliding the point \mathbf{x}_θ along the inscribed curve $\text{Vor}|_e(X) \cap \Sigma$ such that the new triangle candidate satisfies $\rho \leq \bar{\rho}$. Setting $\rho = \bar{\rho}$ leads to a solution for the associated

5 shape-optimal altitude

$$a_\theta = \frac{\|\mathbf{e}_0\|}{2 \tan(\frac{1}{2}\bar{\theta})}, \quad \text{where:} \quad \bar{\theta} = \arcsin\left(\frac{1}{2\bar{\rho}}\right) \quad (7)$$

The position of the points \mathbf{x}_h and \mathbf{x}_θ is calculated by computing the intersection of balls of radius a_h and a_θ , centred at the midpoint of the frontal edge e_0 and the *frontal curve* $\text{Vor}|_e(X) \cap \Sigma$. This approach ensures that new vertices are positioned by advancing a specified distance along the surface Σ in the *frontal* direction. For non-uniform $\bar{h}(\mathbf{x})$, expressions for the position
10 of the point \mathbf{x}_h are non-linear, with the altitude a_h depending on an evaluation of the mesh-size function at the edge midpoints $\bar{h}(\mathbf{m}_i)$ and visa-versa. In practice, since $\bar{h}(\mathbf{x})$ is guaranteed to be sufficiently smooth, a simple iterative predictor-corrector procedure is sufficient to solve these expressions approximately.

Given the set of candidate vertices $\{\mathbf{x}_c, \mathbf{x}_h, \mathbf{x}_\theta\}$, the position of the refinement point \mathbf{x} for the triangle f_i is selected. A *worst-first* strategy is adopted, choosing the point that satisfies local constraints in a greedy fashion. Specifically, the closest
15 point lying on the adjacent Voronoi segment $\text{Vor}|_e(X)$ and outside the neighbourhood of the frontal edge e_0 is selected, with

$$\mathbf{x} = \begin{cases} \mathbf{x}_j, & \text{if } (d_j \leq d_c \text{ and } d_j \geq \frac{1}{2}\|\mathbf{e}_0\|) \\ \mathbf{x}_c, & \text{otherwise} \end{cases}, \quad \text{where:} \quad j = \text{argmin}(d_h, d_\theta). \quad (8)$$

Here, $d_j = \text{dist}(\mathbf{x}_e, \mathbf{x}_j)$ are distances from the midpoint of the frontal edge e_0 to the size- and shape-optimal points \mathbf{x}_h and \mathbf{x}_θ . The cascading selection criteria (8) seeks a balance between local optimality and global convergence, smoothly degenerating to a conventional circumcentre-based Delaunay-refinement strategy in limiting cases, while using locally optimal points where
20 possible. Specifically, these constraints guarantee that refinement points lie within a local *safe* region on the Voronoi complex — being positioned on an adjacent Voronoi segment and bound between the circumcentre of the element itself and the diametric ball of the associated frontal edge. These constraints ensure that new points are never positioned too close to an existing vertex, leading to provable guarantees on the performance of the algorithm. See previous work by the author (Engwirda and Ivers, 2016; Engwirda, 2016b) for additional detail.

25 3.6 Additional remarks

As a *restricted* Delaunay-refinement approach, a full three-dimensional Delaunay tetrahedralisation $\text{Del}(X)$ is incrementally maintained throughout the surface meshing phase, where $X \in \mathbb{R}^3$ is the set of vertices positioned on the surface of the spheroidal geometry. The set of restricted surface triangles $\text{Del}|_\Sigma(X)$ that conform to the underlying spheroidal geometry are expressed as a subset of the tetrahedral faces, such that $\text{Del}|_\Sigma(X) \subseteq \text{Del}(X)$. In an effort to minimise the expense associated with maintaining the full-dimensional topological tessellation, an additional *scaffolding* vertex \mathbf{x}_s is initially inserted
30

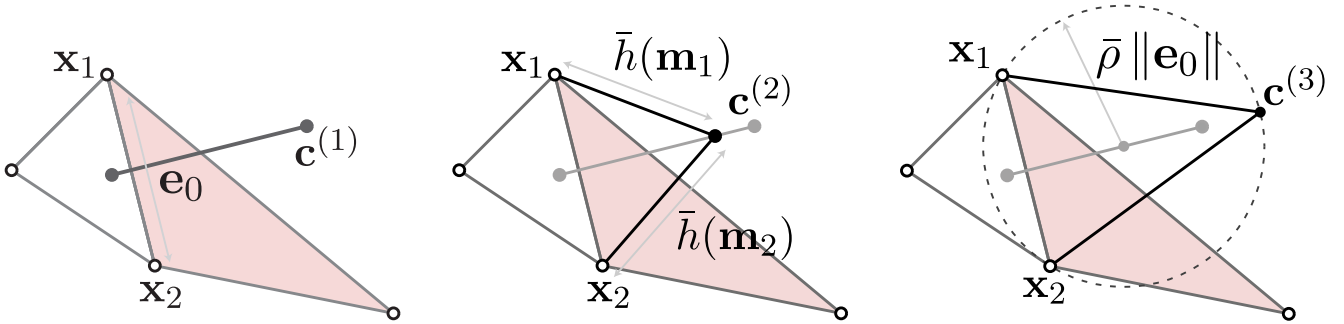


Figure 6. A two-dimensional representation of the off-centre refinement strategies utilised for a given low-quality triangle f_i (shaded), illustrating (a) the *frontal* segment of the Voronoi diagram associated with the short edge $e_0 \in f_i$, (b) placement of the size-optimal vertex x_h such that local size constraints $\bar{h}(x_f)$ are enforced, and (c) placement of a shape-optimal vertex x_θ such that the required radius-edge ratio $\bar{\rho}$ is satisfied.

at the centre of the spheroid. This has the effect of simplifying the resulting topological structure of the interior mesh, with the resulting tetrahedral elements forming a simple *wheel-like* configuration, in which they emanate radially outward from the central scaffolding vertex x_s . See Figure 4 for additional detail.

As per Figure 5, an interesting characteristic of the Frontal-Delaunay algorithm described here relates to the *refinement-trajectory* that is followed when inserting new vertices and triangles. Unlike standard Delaunay-refinement or advancing-front type methods, it can be seen that the algorithm adopts a *space-filling curve* type pattern, covering the surface in a fractal-like configuration, before recursively filling in the gaps. Note that no explicit space-filling curve constraint has been implemented here — this behaviour is simply an emergent property of the algorithm itself, due to interactions between the greedy priority schedule, the frontal filtering and off-centre point-placement strategies. In practice, it has been found that this space-filling type behaviour leads to the construction of very high-quality triangulations, typically exceeding the performance of standard advancing-front type schemes.

4 Hill-climbing mesh optimisation

While the spheroidal Delaunay grids generated using the Frontal-Delaunay refinement algorithm described in Section 3 are guaranteed to be of very high-quality, producing triangulations with angles bounded between $\theta_f = 30$ and $\theta_f = 120$ degrees, these tessellations can often be further improved through subsequent *mesh-optimisation* operations. Recalling that the construction of the *well-centred* grids appropriate for unstructured C-grid schemes *require* that maximum angles be bounded below $\theta_f = 90^\circ$, the application of such optimisation procedures can in fact be seen as a *necessary* component of the grid-generation work-flow for such models.

In the present work, grid-optimisation is realised as a coupled geometrical and topological optimisation task — seeking to reposition vertices and update grid topology to maximise a given element-wise mesh-quality metric $\mathcal{Q}_f(\mathbf{x})$. A *hill-climbing* type optimisation strategy is pursued here, in which a locally-optimal solution is sought based on an initial grid configuration. In this study, the grid is optimised according to the *area-length* quality metric (2.1), a robust scalar measure of grid-quality that achieves a score of +1 for ‘perfect’ elements — decreasing toward zero with increasing levels of element distortion. Optimisation predicates are implemented in a so-called *hill-climbing* fashion (Freitag and Ollivier-Gooch, 1997; Klingner and Shewchuk, 2008), with modifications to the grid accepted only if the local mesh-quality metrics are sufficiently improved. Specifically, a *worst-first* strategy is adopted, in which each given optimisation predicate is required to improve the *worst-case* quality associated with elements in the local subset being acted upon. Such a philosophy ensures that global mesh-quality is increased monotonically as optimisation proceeds. Note that such behaviour is designed to maximise the minimum element quality metric in the grid, rather than improving a mean measure. This represents an important distinction when compared to other iterative mesh-optimisation algorithms, such as Centroidal Voronoi Tessellation (CVT) type schemes (Jacobsen et al., 2013), in which all nodes are typically adjusted simultaneously until a global convergence criterion is satisfied.

4.1 ‘Spring’-based mesh smoothing

Considering firstly the geometric optimality of the grid, a *mesh-smoothing* procedure is undertaken — seeking to reposition the nodes of the grid to improve element quality and mesh-spacing conformance. Following the work of Persson and Strang (2004), a *spring-based* approach is pursued, in which edges in the Delaunay triangulation are treated as *elastic-rods* with a prescribed natural length. Nodes are iteratively repositioned until a local equilibrium configuration is reached. See Algorithm 2 for full details. In the original work of Persson, nodal positions are adjusted via a local time-stepping loop, with all nodes updated concurrently under the action of explicit spring forces. In the current study, a non-iterative variant is employed, in which each node is repositioned one-by-one, such that constraints in each local neighbourhood are satisfied directly. Specifically, a given node \mathbf{x}_i is repositioned as a weighted sum of contributions from incident edges

$$\mathbf{x}_i^{n+1} = \frac{\sum w_k (\mathbf{x}_i^n + \Delta_k \mathbf{v}_k)}{\sum w_k}, \quad \text{where:} \quad \mathbf{v}_k = \mathbf{x}_i^n - \mathbf{x}_j^n, \quad \Delta_k = \frac{\bar{h}(\mathbf{x}_k^n) - l_k}{l_k}. \quad (9)$$

Here, $\mathbf{x}_i^n, \mathbf{x}_j^n$ are the current positions of the two nodes associated with the k -th edge, l_k is the edge length and $\bar{h}(\mathbf{x}_k)$ is the value of the mesh-spacing function evaluated, at the edge midpoint. Δ_k is the relative spring *extension* required to achieve equilibrium in the k -th edge. The scalars $w_k \in \mathbb{R}^+$ are edge weights. Setting $w_k = 1$ results in an unweighted scheme, consisting of simple *linear* springs. In this study, the use of nonlinear weights, defined by setting $w_k = \Delta_k^2$, was found to offer superior performance.

Noting that application of the spring-based operator (9) may move nodes away from the underlying spheroidal surface Σ , an additional *projection* operator is introduced to ensure that the grid conforms to the surface geometry exactly. Following the application of each spring-based adjustment (9), nodes are moved back onto the geometry via a closest-point projection.

Consistent with the hill-climbing paradigm described previously, each nodal adjustment (9) is required to be *validated* before being committed to the updated grid configuration. Specifically, nodal adjustments are accepted only if there is sufficient improvement in the mesh-quality metrics associated with the set of adjacent elements. A sorted comparison of quality metrics

Algorithm 2 Spring and gradient-based node-smoothing

<pre> 1: function NODESMOOTH(\mathbf{x}, Del$_{ \Sigma}(X)$, \bar{Q}) 2: if ($\min(Q(\mathbf{x})) \geq \bar{Q}$) then 3: Call $\{\hat{\mathbf{v}}, \Delta\} \leftarrow \text{SPRINGVEC}(\mathbf{x}, \text{Del}_{ \Sigma}(X))$ to form the <i>spring-based</i> search vector and step-length. 4: else 5: Call $\{\hat{\mathbf{v}}, \Delta\} \leftarrow \text{ASCENTVEC}(\mathbf{x}, \text{Del}_{ \Sigma}(X))$ to form the <i>gradient-based</i> search vector and step-length. 6: end if 7: while ($i \leq M$) do 8: Set $\mathbf{x}' \leftarrow \text{proj}_{ \Sigma}(\mathbf{x} + \Delta^i \hat{\mathbf{v}})$ to move the ver- tex \mathbf{x} along the search vector $\hat{\mathbf{v}}$ and project onto the surface Σ. 9: if ($\text{BETTER}(Q(\mathbf{x}'), Q(\mathbf{x}))$) then 10: Set $\mathbf{x} \leftarrow \mathbf{x}'$ and break. 11: end if 12: Step-length bisection $\Delta^{i+1} \leftarrow \frac{1}{2} \Delta^i$. 13: end while 14: end function </pre>	<pre> 1: function SPRINGVEC(\mathbf{x}, Del$_{ \Sigma}(X)$, $\hat{\mathbf{v}}, \Delta$) 2: Scan edges adj. to \mathbf{x}, calc. $\mathbf{x}' \leftarrow \frac{\sum w_e(\mathbf{x} + \Delta_e \mathbf{e})}{\sum w_e}$, where $w_e \leftarrow \Delta_e^2$ and $\Delta_e \leftarrow \frac{h(\mathbf{x}_e) - \ \mathbf{e}\ }{\ \mathbf{e}\ }$. 3: Set $\mathbf{v} \leftarrow \mathbf{x}' - \mathbf{x}$, $\hat{\mathbf{v}} \leftarrow \frac{\mathbf{v}}{\ \mathbf{v}\ }$ and $\Delta \leftarrow \ \mathbf{v}\$. 4: return search vector $\hat{\mathbf{v}}$ and step-size Δ. 5: end function 1: function ASCENTVEC(\mathbf{x}, Del$_{ \Sigma}(X)$, $\hat{\mathbf{v}}, \Delta$) 2: Scan faces adj. to \mathbf{x} and return the worst adj. element $f \leftarrow \text{argmin}(Q_f(\mathbf{x}))$. 3: Compute the local <i>gradient-ascent</i> search vec- tor $\mathbf{v} \leftarrow \frac{\partial}{\partial \mathbf{x}}(Q_f(\mathbf{x}))$. 4: Solve $Q_f(\mathbf{x}) + \Delta \hat{\mathbf{v}} \cdot \frac{\partial}{\partial \mathbf{x}}(Q_f(\mathbf{x})) \leq \bar{Q}_j(\mathbf{x})$ for the initial step-size Δ, where $\bar{Q}_j(\mathbf{x})$ is the quality of the <i>second-worst</i> triangle adj. to \mathbf{x}. 5: return search vector $\hat{\mathbf{v}}$ and step-size Δ. 6: end function 1: function BETTER(Q', Q) 2: Sort the mesh-quality vectors Q' and Q. 3: return FALSE if any $Q'_i < Q_i$, else TRUE. 4: end function </pre>
---	--

before and after nodal repositioning is performed, with nodal adjustments successful if grid-quality is improved in a *worst-first* manner. This *lexicographical* quality comparison is consistent with the methodology employed in Klingner and Shewchuk (2008).

4.2 Gradient-based mesh smoothing

- 5 While the spring-based mesh-smoothing operator described previously is effective in adjusting a grid to satisfy mesh-spacing constraints, and tends to improve grid-quality on average, it is not guaranteed to improve worst-case element quality metrics in all cases. As such, an additional *steepest-ascent* type optimisation strategy is pursued (Freitag and Ollivier-Gooch, 1997), in which nodal positions are adjusted using the local gradients of incident element quality functions. See Algorithm 2 for full details. Specifically, a given node \mathbf{x}_i is repositioned along a local *search-vector* chosen to improve the quality of the worst
- 10 incident element

$$\mathbf{x}_i^{n+1} = \mathbf{x}_i^n + \Delta_f \hat{\mathbf{v}}_f, \quad \text{where:} \quad \mathbf{v}_f = \frac{\partial}{\partial \mathbf{x}}(Q_f(\mathbf{x}_i)), \quad f = \text{argmin}_j(Q_j(\mathbf{x}_i)). \quad (10)$$

Here, the index j is taken as a loop over the Delaunay triangles $f_j \in \text{Del}|_{\Sigma}(X)$ incident to the node \mathbf{x}_i . The scalar step-length $\Delta_f \in \mathbb{R}^+$ is computed via a line-search along the gradient ascent vector $\hat{\mathbf{v}}_f$, and in this study, is taken as the first value found that leads to a net improvement in the worst-case incident quality metric $\mathcal{Q}_f(\mathbf{x}_i)$. A simple bisection-type strategy is used in the present work, iteratively testing $\Delta_f^p = (\frac{1}{2})^p \alpha$ until a successful nodal adjustment is found. Here p denotes the local line-search iteration. The scalar length $\alpha \in \mathbb{R}^+$ is determined as a solution to the first-order Taylor expansion

$$\mathcal{Q}_f(\mathbf{x}_i) + \alpha \hat{\mathbf{v}}_f \cdot \frac{\partial}{\partial \mathbf{x}} (\mathcal{Q}_f(\mathbf{x}_i)) \leq \tilde{\mathcal{Q}}_j(\mathbf{x}_i). \quad (11)$$

The index j is again taken as a loop over the Delaunay triangles $f_j \in \text{Del}|_{\Sigma}(X)$ incident to the central node \mathbf{x}_i , with the quantity $\tilde{\mathcal{Q}}_j(\mathbf{x}_i)$ representing the *second-lowest* adjacent grid-quality score. This selection strategy (Freitag and Ollivier-Gooch, 1997) is designed to compute an initial displacement α that will improve the worst element in the adjacent set until its quality is equal that of its next best neighbour. Noting that such an expansion is only first-order accurate, the step-length is iteratively decreased using bisection. In this study, a limited line-search is employed, testing iterations $p = \{0, 1, \dots, 5\}$ until a successful step is found. Consistent with the spring-based procedure described previously, a geometry-projection operator is implicitly incorporated within each update (10), ensuring that nodes remain constrained to the spheroidal surface.

4.3 Topological ‘flips’

In addition to purely geometrical operations, general grid optimisation also requires that adjustments be made to the underlying mesh topology, such that the surface triangulation remains a valid Delaunay structure. While it is possible to simply re-compute the full restricted Delaunay topology after each nodal position adjustment, such an approach carries significant computational costs, especially when considering that a majority of nodal position updates involve small perturbations. In this work, an alternative strategy is pursued, based on local element-wise transformations, known as topological *flips*.

For any given pair of adjacent surface triangles $f_i, f_j \in \text{Del}|_{\Sigma}(X)$, a local re-triangulation can be achieved by *flipping* local connectivity about the shared edge x_i, x_j to instead form a new edge between the opposing vertices x_a, x_b . Such an operation results in the deletion of the existing triangles f_i, f_j and the creation of a new pair f'_i, f'_j . This operation is illustrated in Figure 7a. In the present study, the iterative application of such *edge-flipping* operations is used to adjust the topology of the surface triangulation, such that it remains Delaunay. Specifically, given a general, possibly non-Delaunay, surface triangulation $\text{Tri}|_{\Sigma}(X)$, a cascade of edge-flips are used to achieve a valid restricted Delaunay surface tessellation $\text{Del}|_{\Sigma}(X)$. For each adjacent triangle pair $f_i, f_j \in \text{Tri}|_{\Sigma}(X)$ an edge-flip is undertaken if a local violation of the Delaunay criterion is detected. New elements created by successful edge-flips are iteratively re-examined until no further modifications are necessary. This approach follows the standard flip-based algorithms described in, for instance Lawson (1977); Cheng et al. (2013).

Given a triangle $f_i \in \text{Tri}|_{\Sigma}(X)$, the local Delaunay criterion is violated if there exists a node $x_q \notin f_i$ interior to the circumscribing ball associated with the triangle f_i . In this work, violations to the Delaunay criterion are detected by considering the *restricted* circumballs $B(\mathbf{c}_i, r_i)$ associated with each triangle $f_i \in \text{Tri}|_{\Sigma}(X)$, where the ball-centre \mathbf{c}_i is a projection of the *planar* element circumcentre onto the spheroidal surface Σ . Such constructions account for the curvature of the surface. Given an adjacent triangle pair $f_i, f_j \in \text{Tri}|_{\Sigma}(X)$ an edge-flip is undertaken if either opposing vertex x_a, x_b lies within the

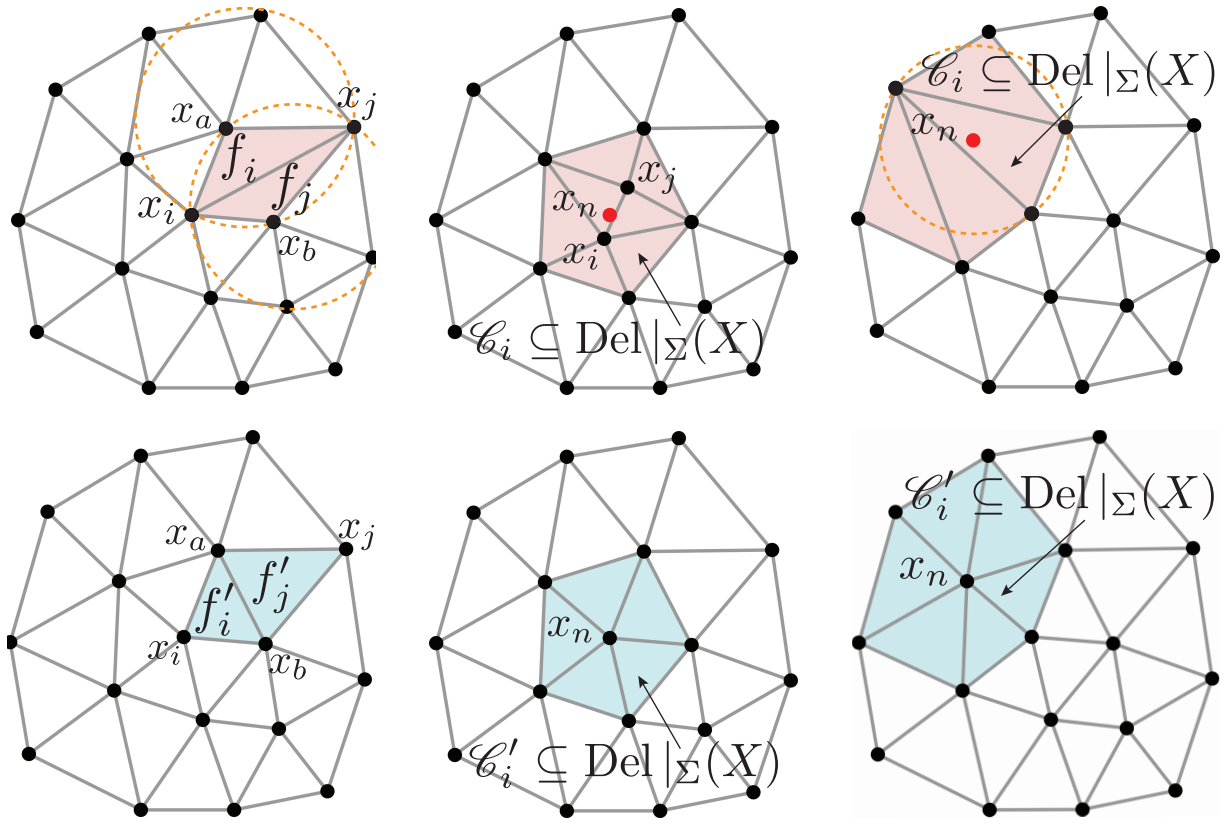


Figure 7. Topological operations for grid optimisation, showing (left) an edge-flip, (middle) an edge-contraction, and (c) an edge-refinement operation. Grid configurations before and after each flip are shown in the upper and lower panels, respectively.

circumball associated with the adjacent triangle. To prevent issues associated with exact floating-point comparisons, a small relative tolerance is incorporated. Specifically, nodes are required to penetrate the opposing circumball by a distance ϵ before an edge-flip is undertaken, with $\epsilon = \frac{1}{2}(r_i + r_j)\bar{\epsilon}$ and $\bar{\epsilon} = 1 \times 10^{-10}$ in the current double-precision implementation.

4.4 Edge contraction

- 5 In some cases, grid-quality and mesh-spacing conformance can be improved through the use of so-called *edge-contraction* operations, whereby nodes are removed from the grid by collapsing certain edges. Given an edge $e_k \in \text{Tri}|_{\Sigma}(X)$, a re-triangulation of the local *cavity* $\mathcal{C}_i \subseteq \text{Tri}|_{\Sigma}(X)$, formed by the set of triangles incident to the nodes $x_i, x_j \in e_k$, can be achieved by *merging* the nodes x_i, x_j at some midpoint along the edge e_k . In addition to collapsing the edge e_k , edge-contraction also removes the two surface triangles $f_i, f_j \in \text{Tri}|_{\Sigma}(X)$ adjacent to e_k , resulting in a new re-triangulation of the local cavity
- 10 $\mathcal{C}'_i \subseteq \text{Tri}|_{\Sigma}(X)$. See Figure 7b for illustration. In the present work, nodes are merged to a mean position \mathbf{x}_n — taken as an average of the adjacent element circumcentres, such that $\mathbf{x}_n = \frac{1}{|\mathcal{C}_i|} \sum \mathbf{c}_j$, where the \mathbf{c}_j 's are centres of the circumballs associated with the adjacent surface triangles $f_j \in \mathcal{C}_i$. The mean position \mathbf{x}_n is projected onto the spheroidal surface Σ . While

Algorithm 3 Hill-climbing grid optimisation

```
1: function OPTIMISE( $\Sigma, \bar{h}(\mathbf{x}), \text{Del}|\Sigma(X)$ )
2:   for ( $i_{\text{outer}} \leq N_{\text{outer}}$ ) do
3:     for ( $i_{\text{inner}} \leq N_{\text{inner}}$ ) do
4:       for ( $\forall$  nodes  $j \in X$ ) do
5:         Call NODESMOOTH( $\mathbf{x}_j, \text{Del}|\Sigma(X)$ )
           to improve geometric distribution of
           triangle vertices.
6:       end for
7:     end for
8:     Call MERGENODE( $\text{Del}|\Sigma(X)$ ) to collapse
           any short edges.
9:     Call SPLITEDGE( $\text{Del}|\Sigma(X)$ ) to refine any
           long edges.
10:    Call EDGEFLIPS( $\text{Del}|\Sigma(X)$ ) to restore grid
           Delaunay-ness (i.e. local-orthogonality).
11:  end for
12:  return surface triangulation object  $\text{Del}|\Sigma(X)$ .
13: end function
1: function EDGEFLIPS( $X, \text{Del}|\Sigma(X)$ )
2:   for ( $\forall$  edges  $e \in \text{Del}|\Sigma(X)$ ) do
3:     Given the adj. triangle-pair  $\mathcal{C} \leftarrow \{f_i, f_j\}$ ,
           flip the common diagonal to re-triangulate
           the cavity  $\mathcal{C}'$ .
4:     if BETTER( $Q(\mathcal{C}'), Q(\mathcal{C})$ ),  $\text{Del}|\Sigma(X) \leftarrow \mathcal{C}'$ .
5:   end for
6: end function
1: function MERGENODE( $X, \text{Del}|\Sigma(X)$ )
2:   for ( $\forall$  edges  $e \in \text{Del}|\Sigma(X)$ ) do
3:     Form a local merge point  $\mathbf{x}'$  about the
           edge  $e$ . Given  $\mathbf{x}_i, \mathbf{x}_j \in e$ , set  $\mathbf{x}' \leftarrow$ 
            $\text{proj}|\Sigma(\frac{1}{|\mathcal{C}|} \sum \mathbf{c}_f)$ , where  $\mathcal{C}$  is the set of tri-
           angles adj. to  $\mathbf{x}_i, \mathbf{x}_j$  and  $\mathbf{c}_f$  are the associ-
           ated circumcentres.
4:     Merge the vertices  $\mathbf{x}_i, \mathbf{x}_j \leftarrow \mathbf{x}'$ , and re-
           triangulate the cavity  $\mathcal{C}'$  as a result.
5:     if BETTER( $Q(\mathcal{C}'), Q(\mathcal{C})$ ),  $\text{Del}|\Sigma(X) \leftarrow \mathcal{C}'$ .
6:   end for
7:   return updated  $X$  and  $\text{Del}|\Sigma(X)$ .
8: end function
1: function SPLITEDGE( $X, \text{Del}|\Sigma(X)$ )
2:   for ( $\forall$  edges  $e \in \text{Del}|\Sigma(X)$ ) do
3:     Form a local refinement point  $\mathbf{x}'$  about the
           edge  $e$ . Given the two adj. triangles,  $\mathcal{C} \leftarrow$ 
            $\{f_i, f_j\}$ , set  $\mathbf{x}'$  equal to the circumcentre of
           the lower quality element.
4:     Append the new vertex  $X \leftarrow \mathbf{x}'$ , and re-
           triangulate the cavity  $\mathcal{C}'$  as a result.
5:     if BETTER( $Q(\mathcal{C}'), Q(\mathcal{C})$ ),  $\text{Del}|\Sigma(X) \leftarrow \mathcal{C}'$ .
6:   end for
7:   return updated  $X$  and  $\text{Del}|\Sigma(X)$ .
8: end function
```

such an approach is slightly more computationally intensive than use of the simple edge-midpoint, the local circumcentre-based strategy has proved to be substantially more effective in practice. Consistent with the hill-climbing philosophy pursued throughout this study, edge-contraction operations are only successful if there is sufficient improvement in the mesh-quality metrics associated with the set of adjacent elements. As per previous discussions, edge-contraction is undertaken based on a

5 lexicographical comparison of the grid-quality vectors associated with the initial and final grid states \mathcal{C}_i and \mathcal{C}'_i , respectively.

4.5 Edge refinement

Fulfilling the opposite role to edge-contraction, so-called *edge-refinement* operations seek to improve grid-quality and mesh-spacing conformance through the addition of new nodes and elements. In the present study, a simplified refinement operation

is utilised, in which a given edge $e_k \in \text{Tri}|_{\Sigma}(X)$ is refined by placing a new node x_n at the centre of the restricted circumball $B(\mathbf{c}_i, r_i)$ associated with the lower quality adjacent triangle $f_i \in \text{Tri}|_{\Sigma}(X)$. Insertion of the new node x_n induces the re-triangulation of a local cavity $\mathcal{C}_i \in \text{Tri}|_{\Sigma}(X)$ — constructed by expanding about x_n in a local greedy fashion. Starting from the initial cavity $\mathcal{C}_i = \{f_i, f_j\}$ adjacent to the edge e_k , additional elements are added in a *breadth-first* manner, with a new, 5 unvisited neighbouring element f_k added to the cavity \mathcal{C}_i if doing so will improve the worst-case element quality metric. The final cavity \mathcal{C}_i is therefore a locally-optimal configuration. In practice, the iterative deepening of \mathcal{C}_i typically convergences in one or two iterations. See Figure 7c for illustration. As per the edge-contraction and node-smoothing operations described previously, edge-refinement is implemented according to a hill-climbing type philosophy, with operations successful only if there is sufficient improvement in local grid-quality. Consistent with previous discussions, a lexicographical comparison of the 10 grid-quality metrics associated with elements in the initial and final states \mathcal{C}_i and \mathcal{C}_i' is used to determine success.

4.6 Optimisation schedule

The full grid optimisation procedure is realised as a combination of the various geometrical and topological operations described previously, organised into a particular iterative optimisation *schedule*. See Algorithm 3 for full details. Each outer iteration consists of a fixed set of operations: four node-smoothing passes, a single pass of edge refinement/contraction operations, and, finally, iterative edge-flipping to restore the Delaunay criterion. In this study, sixteen outer iterations are employed. 15 Each node-smoothing pass is a composite operation, with the spring-based technique used to adjust nodes adjacent to high-quality elements, and the gradient-ascent method used otherwise. Specifically, spring-based smoothing is used to adjust nodes adjacent to elements with a minimum quality score of $\bar{Q}_f \geq 0.9375$. Such thresholding ensures that the expensive gradient-ascent type iteration is reserved for the worst elements in the grid. The optimisation schedule employed here is not based 20 on any rigorous theoretical derivation, but is simply a set of heuristic choices that have proven to be effective in practice. The application of multiple node-smoothing passes within an outer iteration containing subsequent topological, contraction and refinement operations is consistent with the methodologies employed in, for instance Freitag and Ollivier-Gooch (1997); Klingner and Shewchuk (2008).

5 Results & Discussions

25 The performance of the Frontal-Delaunay refinement and hill-climbing optimisation algorithms presented in Sections 3 and 4 was investigated experimentally, with the methods used to mesh a series of benchmark problems. The algorithm was implemented in C++ and compiled as a 64-bit executable. The full algorithm has been implemented as a specialised variant of the general-purpose JIGSAW meshing package, denoted JIGSAW-GEO, and is currently available online (Engwirda, 2016a) or by request from the author. All tests were completed on a Linux platform using a single core of an Intel i7 processor. Visualisation 30 and post-processing was completed using MATLAB.

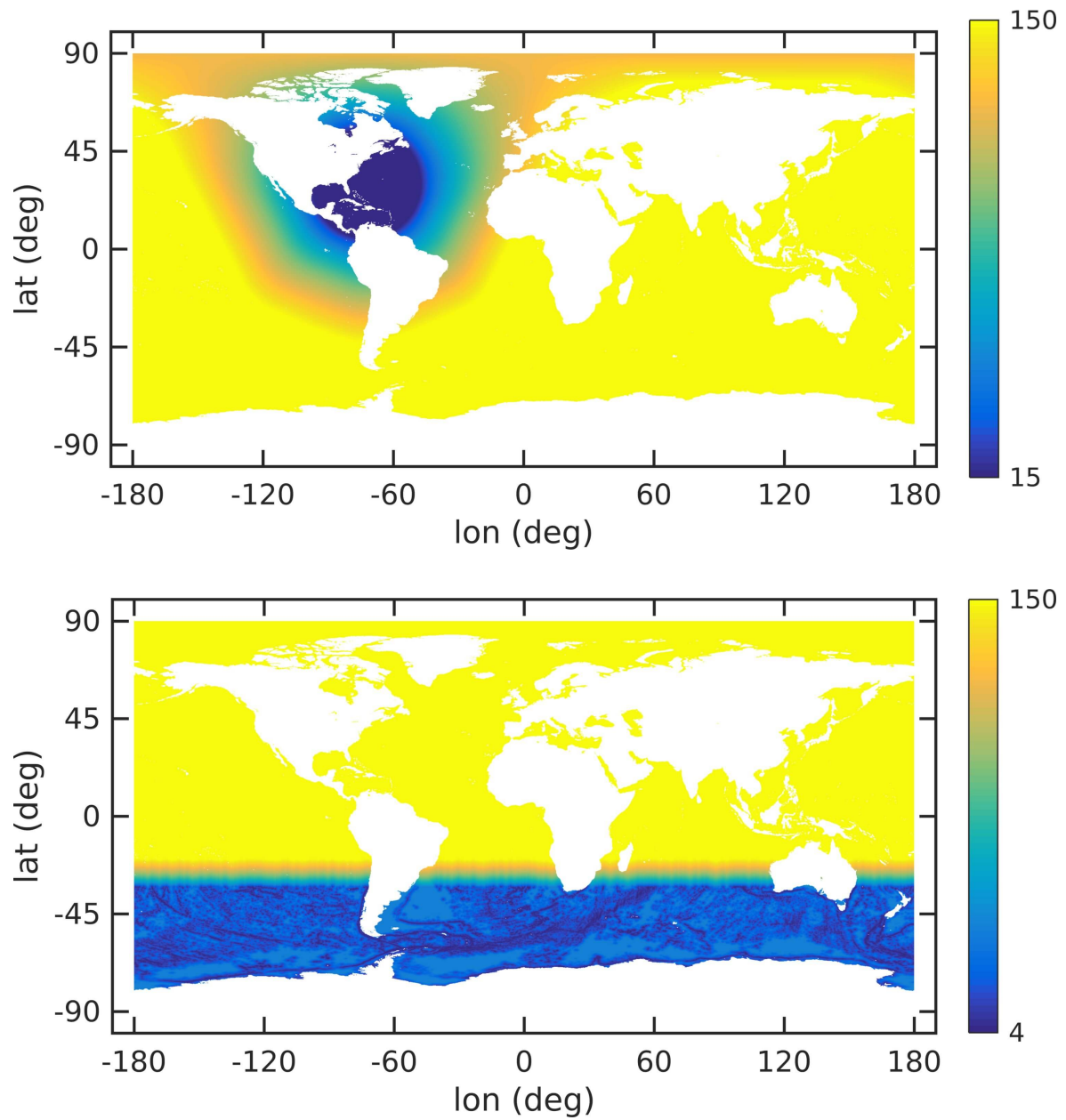


Figure 8. Mesh-spacing functions $\bar{h}(\mathbf{x})$ for the regionally-refined North Atlantic and topographically-refined Southern Ocean grids. Mesh-spacing is shown in km.

5.1 Preliminaries

The JIGSAW-GEO algorithm was used to mesh a set of benchmark problems, suitable for various atmospheric and oceanic general circulation problems. The UNIFORM-SPHERE test-case describes a fixed resolution meshing problem on the sphere, suitable for uniformly resolved atmospheric and/or oceanic studies. The REGIONAL-ATLANTIC test-case describes a simple, regionally-refined grid for global ocean modelling, incorporating a high-resolution, eddy-permitting representation of the North Atlantic ocean basin. Lastly, the SOUTHERN-OCEAN test-case describes a multi-resolution, regionally-refined grid for global ocean simulation, with a very high-resolution representation of the Southern Ocean and Antarctic regions. The mesh-spacing function for this problem was designed using a combination of topographic gradients and regional-refinement. The Voronoi/Delaunay grids for these test-cases are shown in Figures 9, 13, 14 and 16 with associated grid-quality statistics presented in Figures 10, 12 and 15. The underlying mesh-spacing functions used to define the REGIONAL-ATLANTIC and SOUTHERN-OCEAN problems are shown in Figure 8.

In all test cases, limiting radius-edge ratios were specified, such that $\bar{\rho}_f = 1.05$. These constraints ensure that the minimum enclosed angle in any triangle is $\theta_{\min} \geq 28.4^\circ$. For all test problems, detailed statistics on element quality are presented, including histograms of element *area-length ratios* a_f , *element-angles* θ_f , and *relative-edge-length* h_r . The element area-length ratios are robust measures of element quality, where high-quality elements attain scores that approach unity. The relative edge-length metric is defined to be the ratio of the measured edge-length $\|\mathbf{e}\|$ to the target value $\bar{h}(\mathbf{x}_e)$, where \mathbf{x}_e is the edge midpoint. Relative edge-lengths close to unity indicate tight conformance to the imposed mesh-spacing function. High-quality surface triangles contain angles approaching 60° . Histograms further highlight the minimum, maximum and mean values of the relevant distributions as appropriate.

5.2 Uniform global grid

The performance of the JIGSAW-GEO algorithm was first assessed using the UNIFORM-SPHERE test-case, seeking to build a uniformly resolved, staggered Voronoi/Delaunay-type dual grid for general circulation modelling. Spatially uniform mesh-size constraints were enforced, setting $\bar{h}(\mathbf{x}) = 150\text{km}$ over the full sphere. The resulting grid is shown in Figure 9 and contains 83,072 Delaunay triangles and 41,538 Voronoi cells. Grid-quality metrics are presented in Figure 10, showing distributions before and after the application of the grid-optimisation procedure.

Overall, the high quality of the Voronoi/Delaunay grids presented in Figure 9 illustrates the effectiveness of the JIGSAW-GEO algorithm. Based on visual inspection, it is clear that the grids achieve very high levels of geometric quality — being absent of distorted grid-cell configurations and/or areas of over- or under-refinement. Focusing on the distribution of triangle shape-quality explicitly, it is noted that very high levels of mesh regularity are achieved, with the vast majority of element area-length scores tightly clustered about $a_f = 1$. Similarly, the distribution of element angles shows strong convergence around $\theta_f = 60^\circ$, revealing most triangles to be near equilateral. Finally, analysis of the relative-length distributions show that edge-lengths follow the imposed mesh-spacing constraints closely, with very tight clustering about $h_r = 1$.

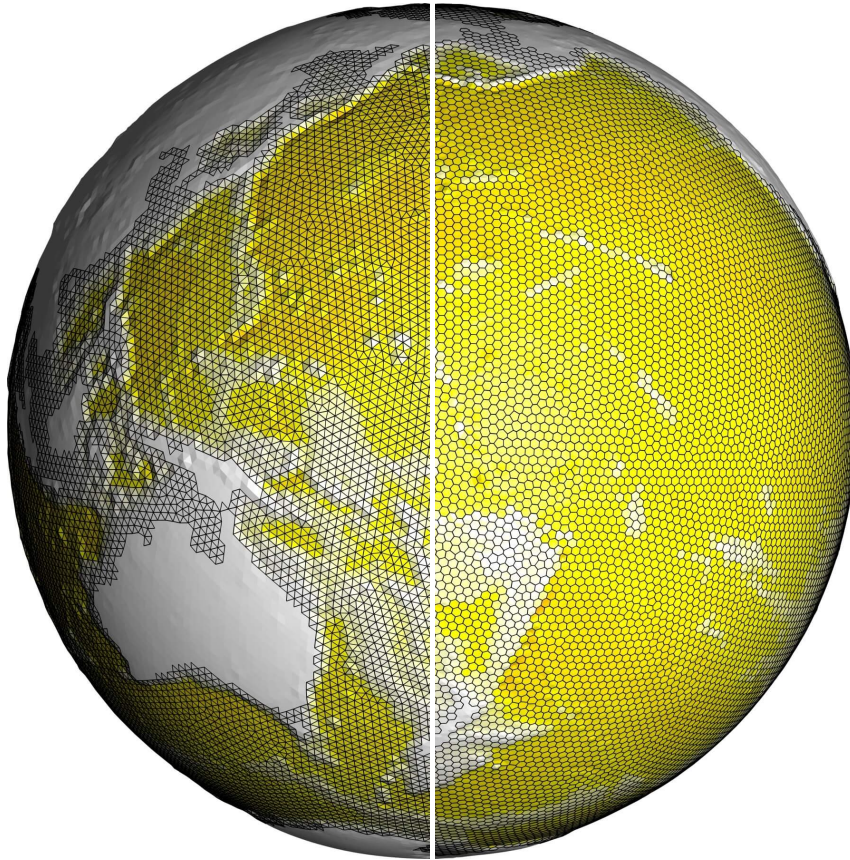


Figure 9. A uniform resolution global grid, showing (left) the underlying spheroidal Delaunay triangulation, and (right) the associated staggered Voronoi dual. 150km grid-spacing was specified globally. Topography is drawn using an exaggerated scale, with elevation from the reference geoid amplified by a factor of 10.

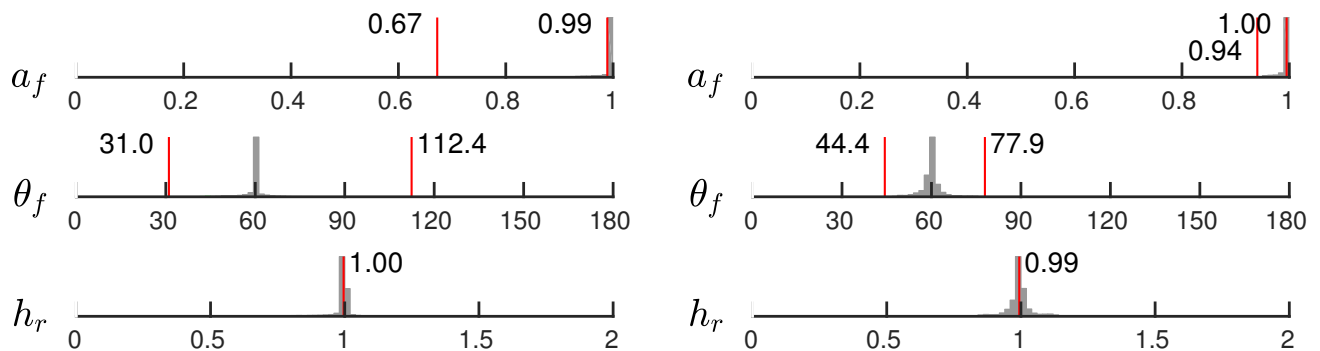


Figure 10. Mesh-quality metrics associated with the uniform resolution global grid, before (left) and after (right) the application of hill-climbing mesh optimisation. Normalised histograms of element area-length ratio a_f , enclosed-angle θ_f and relative-length h_r are illustrated, with minimum, maximum and mean values annotated.

The effect of the grid-optimisation procedure can be assessed by comparing the mesh-quality statistics presented in Figure 10. The application of mesh-optimisation is seen to be most pronounced at the *tails* of the distributions, showing that, as expected, the hill-climbing type procedure is effective at improving the worst elements in the grid. Specifically, the minimum area-length metric is improved from $a_f = 0.67$ to $a_f = 0.94$, and the distribution of element-wise angles is narrowed from $31^\circ \leq \theta_f \leq 112^\circ$ to $44^\circ \leq \theta_f \leq 78^\circ$. A slight broadening of the mean parts of the distributions is also evident, showing that in some cases, higher-quality elements are slightly compromised to facilitate improvements to their lower-quality neighbours. This behaviour is consistent with the *worst-first* philosophy employed in this study.

Beyond improvements to standard grid-quality metrics, the impact of mesh-optimisation can be further understood by considering the so-called *well-centredness* of the resulting staggered Voronoi/Delaunay dual grid. Well-centred triangulations are those for which all element circumcentres are located within their parent triangles, ensuring that the associated Voronoi cells are *nicely-staggered* with respect to the underlying triangulation as a result. Such a constraint is equivalent to requiring that all Delaunay triangles are *acute*, such that $\theta_f \leq 90^\circ$. Further details are outlined in the discussion presented in Section 2.

Well-centred grids are highly desirable from a numerical perspective, allowing, for instance, the mimetic-type C-grid discretisation scheme employed in the MPAS framework to achieve optimal rates of convergence. Specifically, when a grid is well-centred, it is guaranteed that associated edges in the staggered Voronoi and Delaunay cells intersect, ensuring that evaluation of the element-wise transport and circulation terms can be accurately computed using compact numerical stencils. In the case of *perfectly-centred* grids, such intersections occur at edge-midpoints — allowing a numerical scheme based on local linear interpolants to achieve fully second-order accuracy.

The construction of well-centred grids is known to be a difficult problem, and the development of algorithms for their generation is an ongoing area of research (VanderZee et al., 2008; Vanderzee et al., 2010). For the uniform resolution case studied here, it is clear that the hill-climbing type optimisation procedure is successful in generating a well-centred staggered Voronoi/Delaunay dual grid, with all enclosed angles less than 77.9° .

5.3 Regionally-refined North Atlantic grid

The multi-resolution capabilities of the JIGSAW-GEO algorithm were investigated in the REGIONAL-ATLANTIC test-case, seeking to build a regionally-resolved, staggered Voronoi/Delaunay-type dual grid for high-resolution modelling of the North Atlantic ocean basin. Non-uniform mesh-size constraints were enforced, setting $\bar{h}(\mathbf{x}) = 150\text{km}$ globally, with 15km eddy-permitting mesh-spacing specified over the North Atlantic region. The resulting grid is shown in Figure 13 and contains 358,064 Delaunay triangles and 179,081 Voronoi cells. Grid-quality metrics are presented in Figure 12, showing distributions before and after the application of the grid-optimisation procedure.

Consistent with results presented previously, a very high-quality Voronoi/Delaunay grid was generated for the REGIONAL-ATLANTIC problem, with each grid-quality metric tightly clustered about its optimal value, such that $a_f \rightarrow 1$, $\theta_f \rightarrow 60^\circ$ and $h_r \rightarrow 1$. The effect of the grid-optimisation procedure can be assessed by comparing the mesh-quality statistics presented in Figure 12. As per the uniform resolution test-case, mesh-optimisation appears to be most aggressive at the *tails* of the distributions, acting to improve the worst elements in the grid. The minimum area-length metric is improved from $a_f = 0.60$

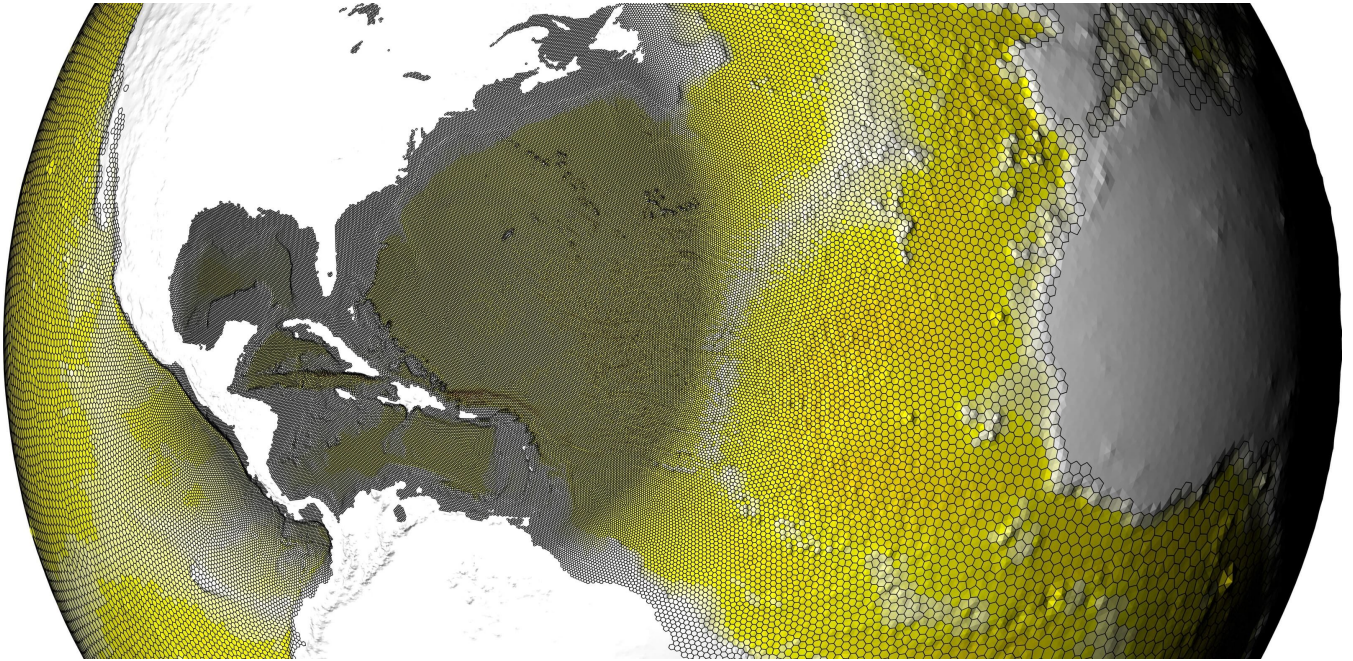


Figure 11. A regionally-refined Voronoi-type grid of the North Atlantic region. Global coarse grid resolution is 150 km, with a 15 km eddy-permitting grid-spacing specified over the Atlantic ocean basin. Topography is drawn using an exaggerated scale, with elevation from the reference geoid amplified by a factor of 10.

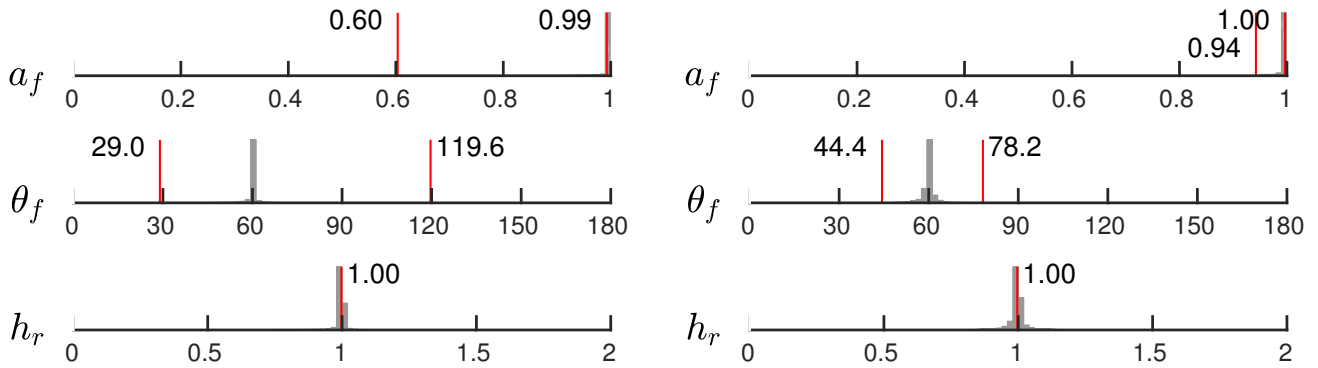


Figure 12. Mesh-quality metrics associated with the regionally-refined Voronoi-type grid of the North Atlantic region, before (left) and after (right) the application of hill-climbing mesh optimisation. Normalised histograms of element area-length ratio a_f , enclosed-angle θ_f and relative-length h_r are illustrated, with minimum, maximum and mean values annotated.

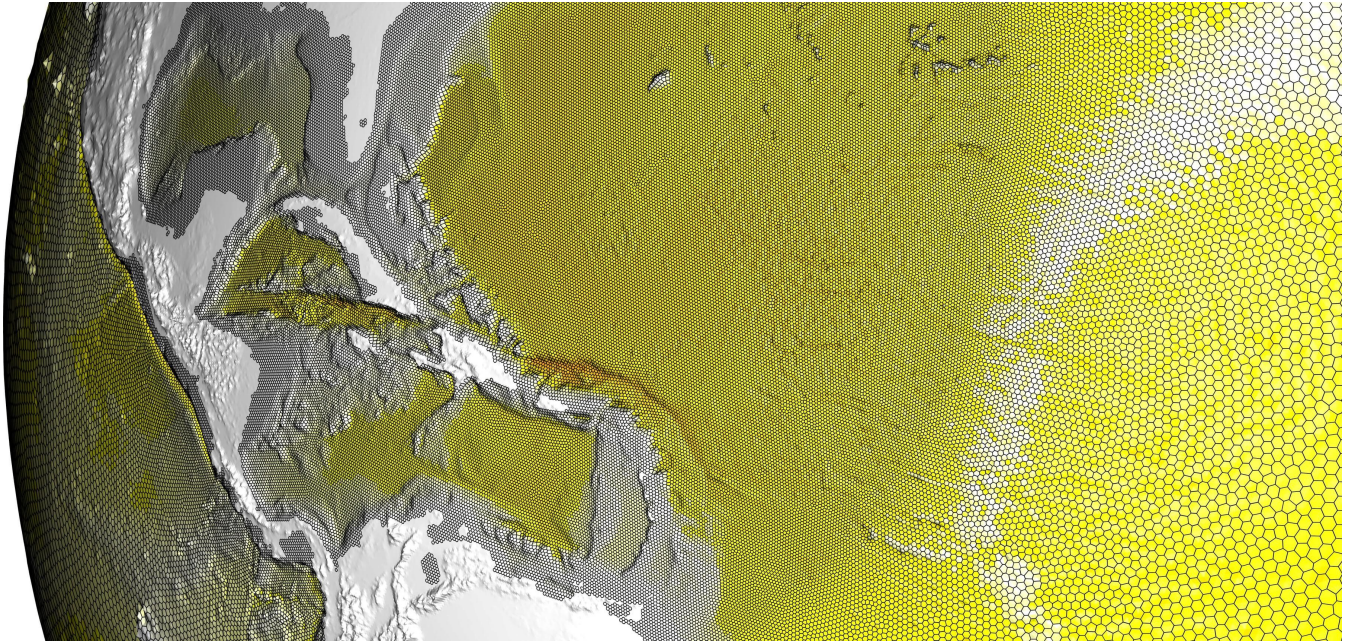


Figure 13. Detail of the regionally-refined Voronoi-type grid of the North Atlantic region. Global coarse grid resolution is 150km, with a 15 km eddy-permitting grid-spacing specified over the Atlantic ocean basin. Topography is drawn using an exaggerated scale, with elevation from the reference geoid amplified by a factor of 10.

to $a_f = 0.94$, and the distribution of element-wise angles is narrowed from $29^\circ \leq \theta_f \leq 120^\circ$ to $44^\circ \leq \theta_f \leq 78^\circ$. The resulting optimised Voronoi/Delaunay staggered grid is also clearly *well-centred*, with all angles in the Delaunay triangulation less than 78.2° . Overall, grid-quality can be seen to achieve essentially the same levels of optimality as the uniform resolution test-case, showing that the JIGSAW-GEO algorithm can be used to generate high-quality spatially-adaptive grids without obvious degradation in mesh-quality.

5.4 Multi-resolution Southern Ocean grid

The JIGSAW-GEO algorithm was then used to mesh the challenging SOUTHERN-OCEAN test-case, allowing its performance for large-scale problems involving rapidly-varying mesh-spacing constraints to be analysed in detail. This test-case seeks to build a multi-resolution, staggered Voronoi/Delaunay-type dual grid for regionally-refined ocean-modelling, with a particular focus on resolution of the Antarctic Circumpolar Current (ACC), and adjacent Antarctic processes. Composite mesh-spacing constraints were enforced, consisting of a coarse global background resolution of 150km, with an *eddy-permitting* 15km grid-spacing specified south of 32.5°S . Additional topographic adaptation is also utilised in the southern annulus region, with grid-resolution increased in regions of large bathymetric gradient. A minimum grid-spacing of 4km was specified. Topographic gradients were computed using the high-resolution ETOPO1 Global Relief dataset (Amante and Eakins, 2009). The resulting grid is shown in Figure 14, with additional detail shown in Figure 16. The grid contains 3,119,849 Delaunay triangles and

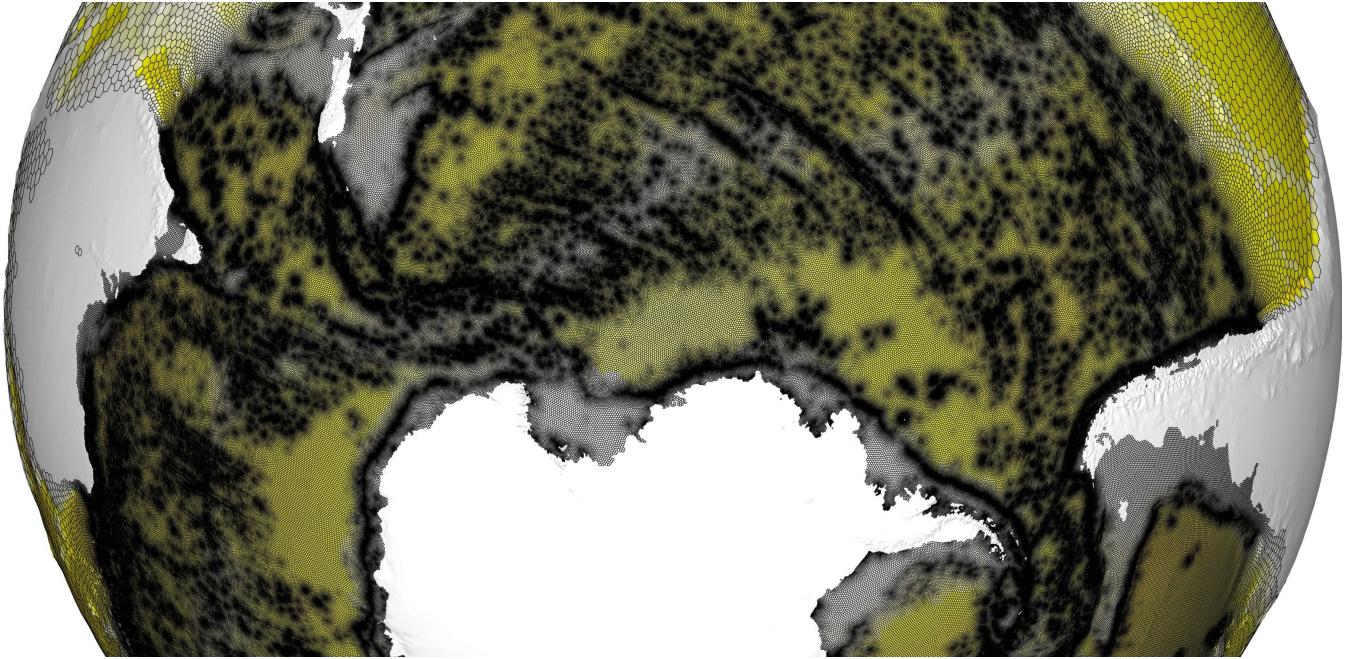


Figure 14. A multi-resolution Voronoi-type grid of the Southern Ocean. Global coarse grid resolution is 150km, with a 15km eddy-permitting grid-spacing specified south of 32.5°S. Additional topographic adaptation is also utilised in the southern annulus region, with grid-resolution increased in areas of large bathymetric gradient. Minimum grid-spacing is 4km. Topography is drawn using an exaggerated scale, with elevation from the reference geoid amplified by a factor of 10.

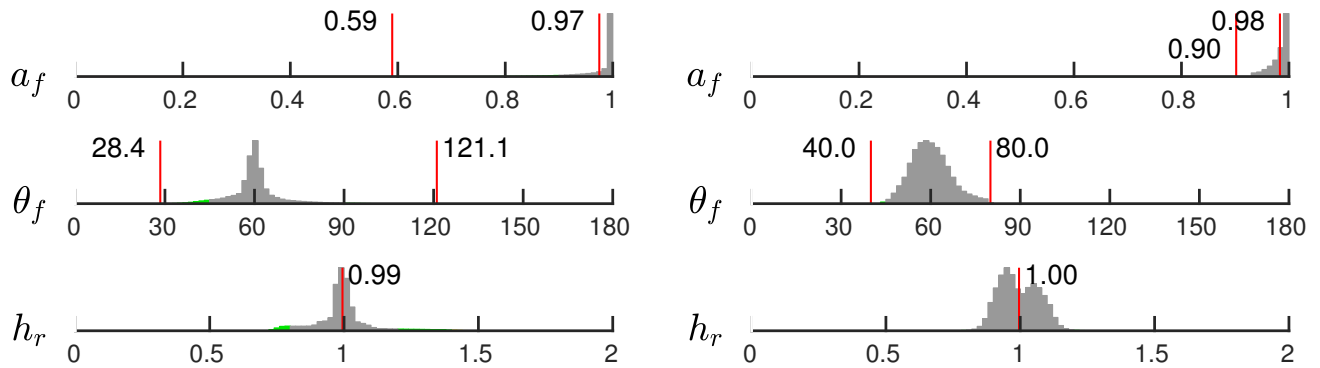


Figure 15. Mesh-quality metrics associated with the multi-resolution Voronoi-type grid of the Southern Ocean, before (left) and after (right) the application of hill-climbing mesh optimisation. Normalised histograms of element area-length ratio a_f , enclosed-angle θ_f and relative-length h_r are illustrated, with minimum, maximum and mean values annotated.

1,559,927 Voronoi cells. Associated grid-quality metrics are presented in Figure 15, showing distributions before and after the application of the grid-optimisation procedure.

Consistent with the uniform resolution test-case presented previously, visual inspection of Figures 14 and 16 confirm that the JIGSAW-GEO algorithm is capable of generating very high quality multi-resolution grids, containing a majority of near-perfect Delaunay triangles and Voronoi cells. Additionally, it can be seen that grid resolution varies smoothly, even in regions of rapidly-fluctuating mesh-spacing constraints, as per the topographically induced refinement patterns shown in Figure 16. Analysis of the grid-quality metrics shown in Figure 15 shows that very high levels of mesh regularity are achieved, with element area-length scores tightly clustered about $a_f = 1$ and element-angles showing strong convergence around $\theta_f = 60^\circ$. Interestingly, despite the complexity of the imposed mesh-spacing function, analysis of the relative-length distribution still shows relatively tight conformance, with a sharp clustering about $h_r = 1$. Overall, mean grid-quality is slightly reduced compared to the uniform resolution case, illustrated by a slight broadening of the grid-quality distributions. Note that such behaviour is expected in the multi-resolution case, with slightly imperfect triangle geometries required to satisfy the non-uniform mesh-spacing constraints. The minimum enclosed-angle in the un-optimised grid can also be seen to lie exactly at the lower angle bound of 28.4° .

The effect of the grid-optimisation procedure can be assessed by comparing the mesh-quality statistics presented in Figure 15. As per the uniform resolution test-case, mesh-optimisation appears to be most aggressive at the *tails* of the distributions, acting to improve the worst elements in the grid. The minimum area-length metric is improved from $a_f = 0.59$ to $a_f = 0.90$, and the distribution of element-wise angles is narrowed from $28^\circ \leq \theta_f \leq 121^\circ$ to $40^\circ \leq \theta_f \leq 80^\circ$. Consistent with previous results, a moderate broadening of the mean components of the distributions can be observed, especially in the enclosed-angle and relative-length metrics. This behaviour shows that, in this case, improvements to worst-case grid-quality are achieved through slight compromises to mean-quality and mesh-spacing conformance, with very high-quality elements being slightly degraded to improve their lower quality neighbours. Note that the resulting optimised Voronoi/Delaunay staggered grid is also *well-centred*, with all angles in the Delaunay triangulation less than 80° . This result shows only a marginal degradation compared to the uniform resolution example presented previously — despite the complexity of the imposed grid-spacing function. This result demonstrates the effectiveness of the optimisation strategies presented here, and shows that very high-quality, well-centred grids can be generated even for general multi-resolution cases. Nonetheless, the construction of well-centred grids remains a challenging task, and it is expected that it may be possible to design test-cases that defeat the current strategy. As such, the pursuit of alternative mesh optimisation strategies, designed to target grid well-centredness directly, is an interesting avenue for future research.

5.5 Computational performance

In addition to the generation of very high-quality grids, the new JIGSAW-GEO algorithm also imposes a relatively moderate computational burden, producing large-scale, multi-resolution grids in a matter of minutes using standard desktop-based computing infrastructure. Specifically, grid-generation for the UNIFORM-SPHERE, REGIONAL-ATLANTIC and SOUTHERN-OCEAN test-cases required 12 seconds, $1\frac{1}{2}$ minutes and 10 minutes of computation time, respectively, running on a single

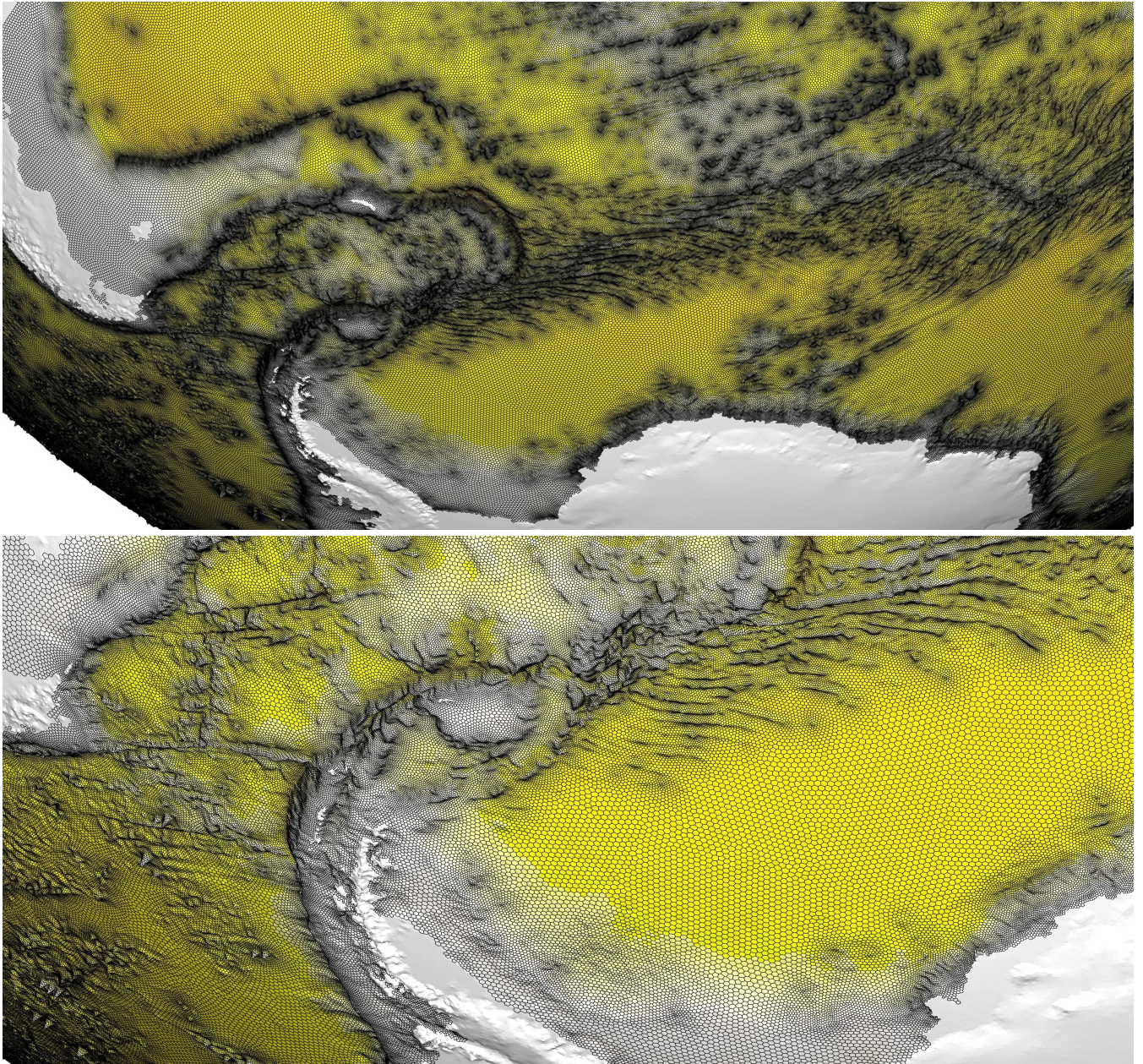


Figure 16. Detail of the multi-resolution Voronoi-type grid of the Southern Ocean. Global coarse grid resolution is 150 km, with a 15 km eddy-permitting grid-spacing specified south of 32.5° S. Additional topographic adaptation is also utilised in the southern annulus region, with grid-resolution increased in areas of large bathymetric gradient. Minimum grid-spacing is 4 km. Topography is drawn using an exaggerated scale, with elevation from the reference geoid amplified by a factor of 10.

core of an Intel i7 processor. In all cases, grid-optimisation was found to be approximately four times as expensive as the initial Frontal-Delaunay refinement. Compared to the existing iterative MPI-SCVT algorithm (Jacobsen et al., 2013), commonly used to generate grids for the MPAS framework, these results represent a significant increase in productivity, with the MPI-SCVT algorithm often requiring days, or even weeks of distributed computing time.

5 Additionally, practical experience with the MPI-SCVT algorithm has shown that it cannot always be relied upon to generate an appropriate grid, irrespective of the amount of computational time allowed for convergence to be reached. While always generating a *locally-orthogonal* and *centroidal* Voronoi tessellation with very high mean grid-quality, the MPI-SCVT algorithm does not provide bounds on worst-case grid-quality. In practice, multi-resolution grids generated using the MPI-SCVT algorithm are often observed to contain a minority of obtuse triangles that violate the *well-centred* constraint, and, due to
10 the nature of the numerical formulation, such grids are inappropriate for use in an unstructured C-grid model such as the MPAS framework. Grid generation for such models often requires a degree of user-driven *trial-and-error* as a result, making grid-generation a somewhat arduous task for model-users. Initial experiments conducted using the JIGSAW-GEO algorithm have shown it to be a useful alternative, reliably generating valid well-centred multi-resolution grids for the MPAS ocean and land-ice frameworks given a wide range of user-defined constraints and configuration settings.

15 6 Conclusions & Future Work

A new algorithm for the generation of multi-resolution staggered unstructured grids for large-scale general circulation modelling on the sphere has been described. Using a combination of Frontal-Delaunay refinement and hill-climbing type optimisation techniques, it has been shown that very high-quality *locally-orthogonal*, *centroidal* and *well-centred* spheroidal grids appropriate for unstructured C-grid type general circulation models can be generated. The performance of this new approach
20 has been verified using a number of multi-scale global benchmarks, including difficult problems incorporating highly non-uniform mesh-spacing constraints.

This new algorithm is available as part of the JIGSAW meshing package, providing a simple and easy-to-use tool for the oceanic and atmospheric modelling communities. A number of global-scale benchmark problems have been analysed, examining the performance of the new approach. The Frontal-Delaunay refinement algorithm has been shown to generate
25 *guaranteed-quality* spheroidal Delaunay triangulations — satisfying worst-case bounds on element-wise angles and exhibiting smooth grading characteristics. This algorithm has been shown to produce very high-quality multi-resolution triangulations, with a majority of elements exhibiting near-perfect conformance to element-shape and grid-spacing based constraints.

The use of a coupled geometrical and topological hill-climbing type optimisation procedure was shown to further improve grid-quality statistics, especially for the lowest quality elements in each mesh. It was demonstrated that these optimisation
30 techniques allow grid-quality to be improved to the extent that fully *well-centred* mesh configurations can be achieved, with all angles in the surface triangulation bounded below 90° . For the three global test-cases presented here, enclosed-angles were bounded above $\theta_f \geq 40^\circ$ and below $\theta_f \leq 80^\circ$.

The construction of locally-orthogonal staggered polygonal grids appropriate for a range of contemporary unstructured C-grid type general circulation models was discussed in detail, with a focus on the generation of multi-resolution grids for the MPAS framework. The availability of this new algorithm is expected to significantly reduce the grid-generation burden for MPAS model-users. Future work will focus on a generalisation of the algorithm and improvements to its efficiency, including: (i) support for inscribed geometrical constraints, such as coastlines, (ii) the use of multi-threaded programming patterns to improve computational performance, and (iii) further enhancements to the mesh optimisation procedures, with a focus on improving the *well-centredness* of the resulting staggered grids. The investigation of *solution-adaptive* multi-scale representations, in which grid-resolution is adapted to spatial variability in model state (Sein et al., 2016), is also an obvious direction for future investigation.

10 *Acknowledgements.* This work was carried out at the NASA Goddard Institute for Space Studies, the Massachusetts Institute of Technology, and the University of Sydney with the support of a NASA–MIT cooperative agreement and an Australian Postgraduate Award. The author wishes to thank Todd Ringler, Luke Van Roekel, Mark Petersen, Matthew Hoffman and Phillip Wolfram for their assistance on grid-generation for the MPAS-O environment. John Marshall provided feedback on an earlier version of the manuscript. The author also wishes to thank the anonymous reviewers for their helpful comments and feedback.

15 7 Code availability

The JIGSAW-GEO grid-generator can be found online at github.com/dengwirda/jigsaw-geo-matlab

Appendix A: Spheroidal Predicates

Recalling the methodology described in Section 3, computation of the *restricted* Delaunay surface tessellation $\text{Del}|_{\Sigma}(X)$ requires the evaluation of a single geometric predicate. Given a spheroidal surface Σ , the task is to compute intersections
 20 between edges in the Voronoi tessellation $\text{Vor}(X)$ and the input features Σ .

A1 Restricted surface triangles

Restricted surface triangles $f_i \in \text{Del}|_{\Sigma}(X)$ are defined as those associated with an *intersecting* Voronoi edge $v_e \in \text{Vor}(X)$, where $v_e \cap \Sigma \neq \emptyset$. These triangles provide a good piecewise linear approximation to the surface Σ . For a given triangle f_i , the associated Voronoi edge v_e is defined as the line-segment joining the two *circumcentres* \mathbf{c}_i and \mathbf{c}_j associated with the pair of
 25 tetrahedrons that share the face f_i . The task then is to find intersections between the line-segments v_e and the surface Σ .

Let \mathbf{p} be a point on a given Voronoi edge-segment v_e

$$\mathbf{p} = \bar{\mathbf{c}} + t\Delta, \quad -1 \leq t \leq +1, \quad \text{where:} \quad \bar{\mathbf{c}} = \frac{1}{2}(\mathbf{c}_i + \mathbf{c}_j), \quad \Delta = \frac{1}{2}(\mathbf{c}_j - \mathbf{c}_i). \quad (\text{A1})$$

Substituting (A1) into the expression for the spheroidal surface (4), the existence of real, bounded solutions, such that $-1 \leq t \leq +1$, indicates a non-trivial intersection $v_e \cap \Sigma \neq \emptyset$. Specifically, expanding and rearranging after substitution

$$\sum_{i=1}^3 \left(\frac{\bar{c}_i + t\Delta_i}{r_i} \right)^2 = 1, \quad \sum_{i=1}^3 \frac{\bar{c}_i^2 + 2t\bar{c}_i\Delta_i + t^2\Delta_i^2}{r_i^2} = 1, \quad \sum_{i=1}^3 \left(\frac{\Delta_i^2}{r_i^2} \right) t^2 + \left(\frac{2\bar{c}_i\Delta_i}{r_i^2} \right) t + \left(\frac{\bar{c}_i^2}{r_i^2} - 1 \right) = 0, \quad (\text{A2})$$

which is simply a quadratic expression for the parameter t and can be solved using the standard approach. Given a real solution

5 $-1 \leq t_\Sigma \leq +1$ the corresponding point of intersection \mathbf{p}_Σ can be found using (A1).

References

- A. Adcroft, J.-M. Campin, C. Hill, and J. Marshall. Implementation of an atmosphere-ocean general circulation model on the expanded spherical cube. *Monthly Weather Review*, 132(12):2845–2863, 2004.
- C. Amante and B. W. Eakins. *ETOPO1 1 arc-minute global relief model: procedures, data sources and analysis*. US Department of Commerce, National Oceanic and Atmospheric Administration, National Environmental Satellite, Data, and Information Service, National Geophysical Data Center, Marine Geology and Geophysics Division, 2009.
- A. Arakawa and V. R. Lamb. Computational design of the basic dynamical processes of the UCLA general circulation model. *Methods in computational physics*, 17:173–265, 1977.
- P.-E. Bernard, N. Chevaugéon, V. Legat, E. Deleersnijder, and J.-F. Remacle. High-order h-adaptive discontinuous Galerkin methods for ocean modelling. *Ocean Dynamics*, 57(2):109–121, 2007.
- R. Bleck. An oceanic general circulation model framed in hybrid isopycnic-cartesian coordinates. *Ocean modelling*, 4(1):55–88, 2002.
- P. B. Bochev and J. M. Hyman. Principles of mimetic discretizations of differential operators. In *Compatible spatial discretizations*, pages 89–119. Springer New York, 2006.
- J. D. Boissonnat and S. Oudot. Provably Good Surface Sampling and Approximation. In *ACM International Conference Proceeding Series*, volume 43, pages 9–18, 2003.
- J. D. Boissonnat and S. Oudot. Provably Good Sampling and Meshing of Surfaces. *Graphical Models*, 67(5):405–451, 2005.
- C. Chen, H. Liu, and R. C. Beardsley. An unstructured grid, finite-volume, three-dimensional, primitive equations ocean model: application to coastal ocean and estuaries. *Journal of atmospheric and oceanic technology*, 20(1):159–186, 2003.
- C. Chen, H. Huang, R. C. Beardsley, H. Liu, Q. Xu, and G. Cowles. A finite volume numerical approach for coastal ocean circulation studies: Comparisons with finite difference models. *Journal of Geophysical Research: Oceans*, 112(C3), 2007.
- S. W. Cheng, T. K. Dey, E. A. Ramos, and T. Ray. Sampling and Meshing a Surface with Guaranteed Topology and Geometry. *SIAM journal on computing*, 37(4):1199–1227, 2007.
- S. W. Cheng, T. K. Dey, and E. A. Ramos. Delaunay Refinement for Piecewise Smooth Complexes. *Discrete & Computational Geometry*, 43(1):121–166, 2010. ISSN 0179-5376. doi:10.1007/s00454-008-9109-3. URL <http://dx.doi.org/10.1007/s00454-008-9109-3>.
- S. W. Cheng, T. K. Dey, and J. R. Shewchuk. *Delaunay Mesh Generation*. Taylor & Francis, New York, 2013.
- R. Comblen, S. Legrand, E. Deleersnijder, and V. Legat. A finite element method for solving the shallow water equations on the sphere. *Ocean Modelling*, 28(1):12–23, 2009.
- C. J. Conroy, E. J. Kubatko, and D. W. West. ADMESH: An advanced, automatic unstructured mesh generator for shallow water models. *Ocean Dynamics*, 62(10-12):1503–1517, 2012.
- Q. Du, V. Faber, and M. Gunzburger. Centroidal Voronoi tessellations: applications and algorithms. *SIAM review*, 41(4):637–676, 1999.
- H. Edelsbrunner and N. R. Shah. Triangulating Topological Spaces. *International Journal of Computational Geometry & Applications*, 7(04):365–378, 1997.
- D. Engwirda. Multi-resolution unstructured grid-generation for geophysical applications on the sphere. *arXiv preprint arXiv:1512.00307*, 2015.
- D. Engwirda. JIGSAW-GEO: Grid-generation for general circulation modelling on the sphere. <http://www.github.com/dengwirda/jigsaw-geo-matlab>, 2016a.
- D. Engwirda. Conforming restricted Delaunay mesh generation for piecewise smooth complexes. *Procedia Engineering*, 163:84–96, 2016b.

- D. Engwirda and D. Ivers. Off-centre Steiner points for Delaunay-refinement on curved surfaces. *Computer-Aided Design*, 72:157 – 171, 2016. ISSN 0010-4485. doi:http://dx.doi.org/10.1016/j.cad.2015.10.007. URL http://www.sciencedirect.com/science/article/pii/S0010448515001608. 23rd International Meshing Roundtable Special Issue: Advances in Mesh Generation.
- H. Erten and A. Üngör. Quality Triangulations with Locally Optimal Steiner Points. *SIAM J. Sci. Comp.*, 31(3):2103–2130, 2009.
- 5 R. Ford, C. Pain, M. Piggott, A. Goddard, C. De Oliveira, and A. Umpleby. A nonhydrostatic finite-element model for three-dimensional stratified oceanic flows. Part I: model formulation. *Monthly Weather Review*, 132(12):2816–2831, 2004a.
- R. Ford, C. Pain, M. Piggott, A. Goddard, C. de Oliveira, and A. Umpleby. A nonhydrostatic finite-element model for three-dimensional stratified oceanic flows. Part II: model validation. *Monthly weather review*, 132(12):2832–2844, 2004b.
- L. A. Freitag and C. Ollivier-Gooch. Tetrahedral mesh improvement using swapping and smoothing. *International Journal for Numerical*
 10 *Methods in Engineering*, 40(21):3979–4002, 1997.
- P. J. Frey and P.-L. George. *Mesh generation: application to finite-elements*. ISTE, 2007.
- O. Fringer, M. Gerritsen, and R. Street. An unstructured-grid, finite-volume, nonhydrostatic, parallel coastal ocean simulator. *Ocean Modelling*, 14(3):139–173, 2006.
- C. Geuzaine and J.-F. Remacle. Gmsh: A 3-D finite element mesh generator with built-in pre-and post-processing facilities. *International*
 15 *Journal for Numerical Methods in Engineering*, 79(11):1309–1331, 2009.
- R. Heikes and D. A. Randall. Numerical integration of the shallow-water equations on a twisted icosahedral grid. Part I: Basic design and results of tests. *Monthly Weather Review*, 123(6):1862–1880, 1995.
- R. Holleman, O. Fringer, and M. Stacey. Numerical diffusion for flow-aligned unstructured grids with application to estuarine modeling. *International Journal for Numerical Methods in Fluids*, 72(11):1117–1145, 2013.
- 20 D. Jacobsen, M. Gunzburger, T. Ringler, J. Burkardt, and J. Peterson. Parallel algorithms for planar and spherical Delaunay construction with an application to centroidal Voronoi tessellations. *Geoscientific Model Development*, 6(4):1353–1365, 2013.
- C. Jamin, P. Alliez, M. Yvinec, and J.-D. Boissonnat. CGALmesh: a generic framework for delaunay mesh generation. *ACM Transactions on Mathematical Software (TOMS)*, 41(4):23, 2015.
- B. M. Klingner and J. R. Shewchuk. Aggressive tetrahedral mesh improvement. In *Proceedings of the 16th international meshing roundtable*,
 25 pages 3–23. Springer, 2008.
- Z. Lai, C. Chen, G. W. Cowles, and R. C. Beardsley. A nonhydrostatic version of FVCOM: 1. Validation experiments. *Journal of Geophysical Research: Oceans*, 115(C11), 2010.
- J. Lambrechts, R. Comblen, V. Legat, C. Geuzaine, and J.-F. Remacle. Multiscale mesh generation on the sphere. *Ocean Dynamics*, 58(5-6): 461–473, 2008.
- 30 C. L. Lawson. Software for C^1 Surface Interpolation. In J. R. Rice, editor, *Mathematical Software III*, pages 161–194. Academic Press, New York, 1977.
- K. Lipnikov, G. Manzini, and M. Shashkov. Mimetic finite difference method. *Journal of Computational Physics*, 257:1163–1227, 2014.
- R. Löhner. Regridding surface triangulations. *Journal of Computational Physics*, 126(1):1–10, 1996.
- G. Madec et al. NEMO ocean engine. 2015.
- 35 J. Marshall, A. Adcroft, C. Hill, L. Perelman, and C. Heisey. A finite-volume, incompressible Navier-Stokes model for studies of the ocean on parallel computers. *Journal of Geophysical Research*, 102:5753–5766, 1997.
- R. J. Murray. Explicit generation of orthogonal grids for ocean models. *Journal of Computational Physics*, 126(2):251–273, 1996.

- C. Pain, M. Piggott, A. Goddard, F. Fang, G. Gorman, D. Marshall, M. Eaton, P. Power, and C. De Oliveira. Three-dimensional unstructured mesh ocean modelling. *Ocean Modelling*, 10(1):5–33, 2005.
- P.-O. Persson. Mesh Size Functions for Implicit Geometries and PDE-based Gradient Limiting. *Engineering with Computers*, 22(2):95–109, 2006. ISSN 0177-0667. doi:10.1007/s00366-006-0014-1. URL <http://dx.doi.org/10.1007/s00366-006-0014-1>.
- 5 P.-O. Persson and G. Strang. A simple mesh generator in MATLAB. *SIAM review*, 46(2):329–345, 2004.
- M. Piggott, G. Gorman, C. Pain, P. Allison, A. Candy, B. Martin, and M. Wells. A new computational framework for multi-scale ocean modelling based on adapting unstructured meshes. *International Journal for Numerical Methods in Fluids*, 56(8):1003–1015, 2008.
- W. M. Putman and S.-J. Lin. Finite-volume transport on various cubed-sphere grids. *Journal of Computational Physics*, 227(1):55–78, 2007.
- D. A. Randall, T. D. Ringler, R. P. Heikes, P. Jones, and J. Baumgardner. Climate modeling with spherical geodesic grids. *Computing in Science and Engineering*, 4(5):32–41, 2002.
- 10 S. Rebay. Efficient Unstructured Mesh Generation by Means of Delaunay Triangulation and Bowyer-Watson Algorithm. *Journal of Computational Physics*, 106(1):125 – 138, 1993. ISSN 0021-9991. doi:<http://dx.doi.org/10.1006/jcph.1993.1097>. URL <http://www.sciencedirect.com/science/article/pii/S0021999183710971>.
- T. Ringler, L. Ju, and M. Gunzburger. A multiresolution method for climate system modeling: application of spherical centroidal Voronoi tessellations. *Ocean Dynamics*, 58(5-6):475–498, 2008.
- 15 T. Ringler, J. Thuburn, J. B. Klemp, and W. C. Skamarock. A unified approach to energy conservation and potential vorticity dynamics for arbitrarily-structured C-grids. *Journal of Computational Physics*, 229(9):3065–3090, 2010.
- T. Ringler, M. Petersen, R. L. Higdon, D. Jacobsen, P. W. Jones, and M. Maltrud. A multi-resolution approach to global ocean modeling. *Ocean Modelling*, 69:211–232, 2013.
- 20 D. Ryppl and P. Krysl. Triangulation of 3D surfaces. *Engineering with Computers*, 13(2):87–98, 1997.
- J. Schreiner, C. E. Scheidegger, S. Fleishman, and C. T. Silva. Direct (re) meshing for efficient surface processing. In *Computer graphics forum*, volume 25, pages 527–536. Wiley Online Library, 2006.
- D. V. Sein, S. Danilov, A. Biastoch, J. V. Durgadoo, D. Sidorenko, S. Harig, and Q. Wang. Designing variable ocean model resolution based on the observed ocean variability. *Journal of Advances in Modeling Earth Systems*, 8(2):904–916, 2016. ISSN 1942-2466. doi:10.1002/2016MS000650. URL <http://dx.doi.org/10.1002/2016MS000650>.
- 25 W. C. Skamarock, J. B. Klemp, M. G. Duda, L. D. Fowler, S.-H. Park, and T. D. Ringler. A multiscale nonhydrostatic atmospheric model using centroidal Voronoi tessellations and C-grid staggering. *Monthly Weather Review*, 140(9):3090–3105, 2012.
- E. VanderZee, A. N. Hirani, D. Guoy, and E. Ramos. Well-centered planar triangulation—an iterative approach. In *Proceedings of the 16th International Meshing Roundtable*, pages 121–138. Springer, 2008.
- 30 E. Vanderzee, A. N. Hirani, D. Guoy, and E. A. Ramos. Well-centered triangulation. *SIAM Journal on Scientific Computing*, 31(6):4497–4523, 2010.
- S. Vitousek and O. B. Fringer. A nonhydrostatic, isopycnal-coordinate ocean model for internal waves. *Ocean Modelling*, 83:118–144, 2014.
- Q. Wang, S. Danilov, D. Sidorenko, R. Timmermann, C. Wekerle, X. Wang, T. Jung, and J. Schröter. The Finite Element Sea Ice-Ocean model (FESOM) v.1.4: formulation of an ocean general circulation model. *Geoscientific Model Development*, 7(2):663–693, 2014. doi:10.5194/gmd-7-663-2014. URL <http://www.geosci-model-dev.net/7/663/2014/>.
- 35